Title

Assessment of Bubble Pump Model for Fluid Directional Motion from Asymmetric Heated Ratchets in Nucleate Boiling Regime

Author

Gutta Prudhvi Reddy, FNU

Publication Date

2024

Peer reviewed|Thesis/dissertation

Assessment of Bubble Pump Model for Fluid Directional Motion from Asymmetric Heated Ratchets in Nucleate Boiling Regime

By

GUTTA PRUDHVI REDDY

DISSERTATION

Submitted in partial satisfaction of the requirements for the degree of

MASTER OF SCIENCE

in

Mechanical and Aerospace Engineering

in the

OFFICE OF GRADUATE STUDIES

of the

UNIVERSITY OF CALIFORNIA

DAVIS

Approved:

Vinod Narayanan, Chair

Paul A. Erickson

Stephen K. Robinson

Committee in Charge

2024

ABSTRACT

Passive two-phase fluid cooling systems are of major interest for cooling electronics in terrestrial and micro gravity environments due to their compactness and minimization of moving parts. In this thesis, the use of asymmetry for bubble ebullition and growth on a heated surface to passively generate lateral motion of fluid within an open-ended channel is discussed. The asymmetry is achieved by locating reentrant slot cavities on one face of a mm-scale 30/60-degree ratchet. Two such ratcheted walls with cavities in every third ratchet form the vertical walls of an open-ended channel. The ratcheted walls are heated using a serpentine thick-film metallic heater. The open-ended channel is located within a quiescent pool of a dielectric fluid. Visualization studies show that bubbles and slugs tend to move in a preferential direction within the open channel. This direction corresponds to the 30-degree slope face of the ratchet, in which the reentrant cavity is located. Prior studies have alluded to two potential mechanisms for this preferential lateral motion- (1) bubble pump model developed by Kapsenberg et al. [14], which attributes the lateral motion to the momentum imparted by the growing bubble to the surrounding liquid, and (2) asymmetry in the curvature of the slug that spans several ratchet lengths, resulting in a net surface tension force along the 30-degree slope of the ratchet. In order to assess the importance of the bubble pump model, bubble ebullition and growth from the nucleation sites for different heat fluxes and subcooling temperatures are captured using high speed videos and are analyzed using custom image processing of high-speed videos. The major purpose of the image processing is to detect the bubbles in the frames and obtain height and diameter of the bubbles attached to the ratchet in each frame. Active contouring and segmentation techniques are used to detect bubbles in the frames. The velocity imparted by the growing bubble on the ratchet to the surrounding liquid is calculated using this data with the semi empirical model of Kapsenberg et al. This predicted velocity is compared against velocities of detached small (Stokes) bubbles in the field of view obtained using particle (bubble) tracking velocimetry. This comparative analysis has revealed that

the semi empirical formula predicts the horizontal velocity imparted by the growing bubble on the ratchet with a deviation of ±15% of the horizontal velocity obtained from the particle tracking velocimetry except for high subcooling mid heat flux condition. Overall, it was observed that around 20-30 mm/s of lateral velocity is imparted in the surrounding fluid by the bubble growing on ratchet. These results validate the bubble pumping model and the semi empirical formula developed by Kapsenberg in the nucleate boiling regime.

ACKNOWLEDGEMENTS

I extend my deepest gratitude to my advisor, Dr. Vinod Narayanan, for providing me with the opportunity to work on this fascinating project. I am profoundly grateful for his guidance and unwavering support throughout the journey of completing this thesis. His insightful feedback and constructive criticism have been instrumental in shaping the direction and content of this research, and I consider myself incredibly fortunate to be his student.

I would like to express my appreciation to my committee members, Dr. Paul A. Erickson, and Dr. Stephen K. Robinson, for their time and effort in reviewing this dissertation and serving on my committee.

I am also thankful to the University of California Davis for providing access to resources and facilities that have been essential for the successful completion of this thesis. The Mechanical and Aerospace Engineering department has been a nurturing academic environment, and I am grateful for the opportunities it has offered for intellectual growth.

The success of this project is also attributed to the tremendous support of my past lab mates, Ramuel Safarkoolan and Raymond Odele. A special thanks to them for leaving me with a fully designed experimental setup and the high-speed images used for the analysis.

Lastly, I want to express my profound gratitude to my family and friends for their unwavering support, understanding, and encouragement. Their love and belief in me have been a constant source of motivation.

Financial assistance for the project provided by NSF under Grant 1740515 and 1740506 is gratefully acknowledged.

Table of Contents

List of Tables

List of Figures

CHAPTER 1 INTRODUCTION

Advancements in Artificial Intelligence (AI) and Machine Learning (ML) are pushing the limits of power density in electronics for larger and faster computations. This increase in power density and the smaller form factor of electronics has resulted in the need for higher heat dissipation in a smaller volume, challenging the limits of current heat removal techniques. The next generation of electronics requires more innovative and efficient heat removal techniques beyond the currently available methods, such as natural convection, forced convection using fans and blowers, heat sinks, and single-phase cooling.

Phase change heat transfer, such as boiling and evaporation, could offer a viable solution for addressing higher heat fluxes. The key advantage of phase change heat transfer lies in the utilization of the latent heat of vaporization of the fluid as a heat sink at a constant saturation temperature. In most cases, the energy required to convert liquid to vapor exceeds the sensible heat of the liquid. For a one-degree change in temperature, 4.217 kJ/kg of heat must be either removed from or added to water at atmospheric pressure, while 2257 kJ/kg of heat must be added to induce a phase change in water [1]. Using a fluid with an appropriate boiling point in a phase change process can effectively remove higher heat fluxes than the currently available heat removal techniques, while maintaining a constant surface temperature.

The heat fluxes that can be attainable with various common heat transfer mechanisms are shown in Figure 1-1. Higher heat fluxes with lower temperature difference between the surface of device and the surrounding medium can be obtained as we transition from natural air convection to the immersion boiling fluorocarbons. This underscores the viability of phase change heat transfer as a solution for cooling next-generation electronics.

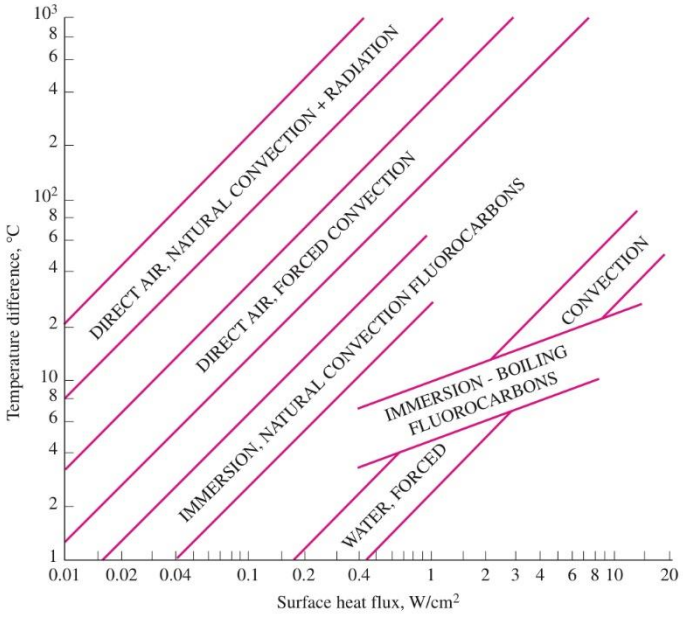

Figure 1-1: Heat fluxes that can be attained at specific temperature difference between surface of device and the surrounding fluid with various heat transfer mechanisms [2]

Phase change heat transfer involving boiling as shown in Figure 1-2 is classified into pool boiling and flow boiling, based on the presence of bulk fluid motion. In pool boiling, the fluid is stationary, and any bubble movement is a result of natural buoyancy convection. On the other hand, in flow boiling, external means such as pumps force the fluid to move. Both pool boiling and flow boiling are further categorized into subcooled boiling and saturated boiling based on the bulk liquid temperature. If the liquid temperature during boiling is below the saturation temperature, it is considered subcooled. If it is equal to the saturation temperature, it is classified as saturated [2].

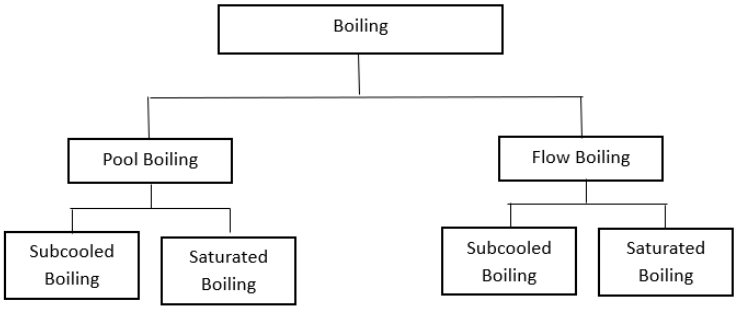

Figure 1-2: Classification of phase change heat transfer involving boiling.

1.1 Boiling Curve

Boiling is a widely applied and familiar heat transfer mechanism in the industry involving heating and cooling. The pioneering work to understand pool boiling was conducted in 1934 by S. Nukiyama using electrically heated nichrome and platinum wires immersed in liquid. He observed four different regimes based on the heating of the wire: natural free convection boiling (up to point A), nucleate boiling (from A to C), transition boiling (from C to D), and film boiling (from D) as illustrated in Fig.1-3. ΔT_w represents the temperature difference between the heating surface and the saturation temperature of liquid, and q'' refers to the heat flux from the wire based on the current and voltage across the wire. Good performance is achieved with higher heat fluxes at lower temperatures of the heating surface [2].

Incropera et al.[1] and Carey [3] provide a detailed description of each of these regimes in the pool boiling. For the free convection, the surface temperature should be a bit higher than the saturation temperature so that the bubble formation will be sustained. During this regime the heat transfer is mostly due to the free convection effects. As the temperature is increased, the nucleation regime is reached which is further divided into isolated bubble regime (A to B) and the jets and columns regime (B to C). This regime is mainly characterized by nucleation of bubbles, bubble growth, bubble departure and coalescence. In the isolated bubble regime, the bubbles start growing and depart from the nucleation sites into the liquid. This departure from the surface induces the mixing near the surface and increases the heat transfer. In the jets and columns nucleate boiling regime, the widespread coalescence of bubbles near the surface inhibits fluid flow, subsequently reducing the heat transfer (point B in figure 1-3). However, the increase in wall superheat maintains the trend of the increasing heat flux until the reduction in convective effects is balanced by the increasing wall superheat. The heat flux at this point is the Critical Heat Flux in the nucleate boiling regime. Because of the high heat flux and low required wall superheat associated with nucleate boiling, this is a desirable operating regime for optimized cooling.

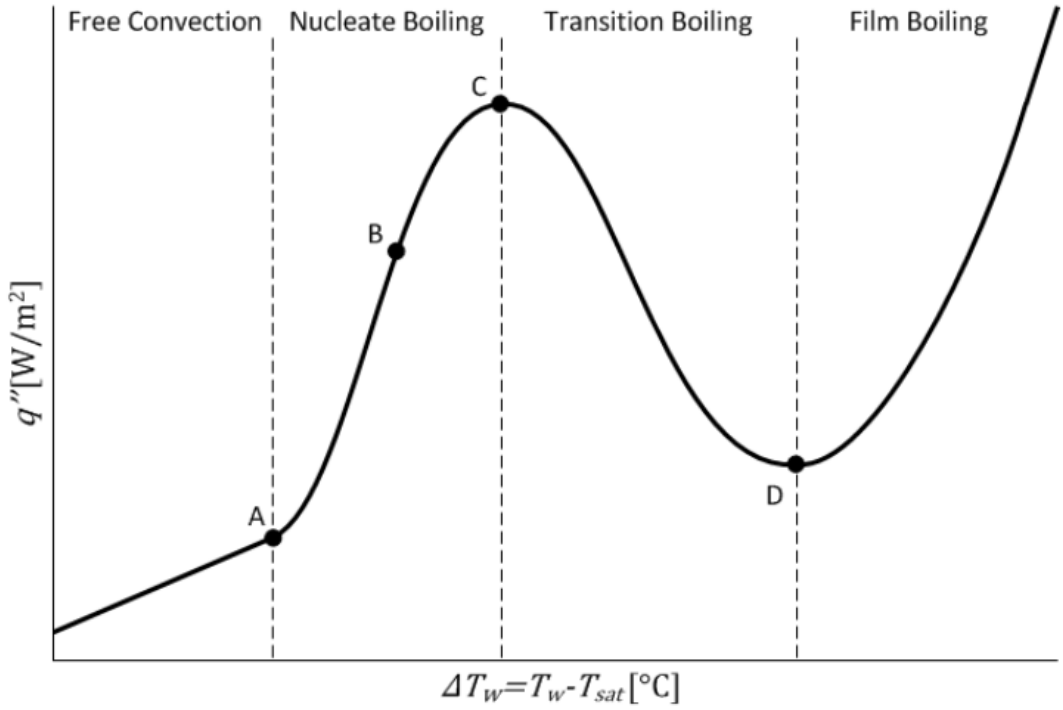

Figure 1-3: Typical Boiling curve of water at 1 atm [2], (T_w = surface temperature)

With a further increase in the temperature, bubble formation becomes so rapid that a vapor film or a blanket begins to form on the surface. This regime is called transition boiling, as conditions may oscillate between nucleate boiling and film boiling at any point on the surface. As the thermal conductivity of the vapor is very low, the heat transfer in this regime is reduced. Film boiling occurs when the entire surface is covered with a stable vapor film, and no liquid touches the surface. The point with the minimum heat transfer at which film boiling starts (D) is referred to as the Leidenfrost regime. Heat transfer from surface to liquid occurs by conduction and radiation through vapor in this regime.

Significant research efforts have been dedicated to the development of technologies and methods aimed at enhancing heat transfer within two-phase flows. These methodologies can broadly be classified into two categories: active and passive. Active heat transfer method utilizes external power sources, such as pumps, vibration, or magnetic fields, while the passive heat transfer methods leverage on fluid properties

and surface enhancements. Due to the high cost and complexity with active methods, there has been a great emphasis on the exploration and development of passive methods for two-phase flows in the research [4].

1.2 Passive methods for phase change heat transfer

The primary focus of this thesis is to develop a novel design for passive transport of fluid in boiling heat transfer. To understand the potential of the research, this section covers the existing technologies for the pumpless fluid transport in the two-phase flows.

1.2.1 Heat Pipes

Heat pipes are one of the most efficient passive heat transfer methods using two phase flow. They consist of a working fluid in hermetically sealed tubes or vessels. Heat is applied at one end of this tube leading to the vaporization of the fluid at a constant temperature (evaporator section). This gaseous fluid, due to the pressure difference across the pipe, reaches the other end where the gaseous fluid is condensed back to the liquid form (condenser section). The wicking structure in the heat pipe provides capillary pressure, causing the liquid to flow back to the evaporator. Figure 1-4 shows the schematic of the heat pipe [5] . With simple operational principle, no moving parts and strong heat transfer ability, heat pipes are widely used in the electronic systems, solar energy systems, isothermal reactors etc. [6].

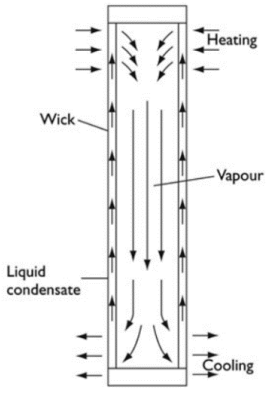

Figure 1-4: Schematic of the heat pipe. The heating location represents the evaporator section, and the cooling location represents the condenser section [5]

Voigt et al. [7] conducted preliminary investigations on the heat pipe to understand its heat transfer properties using a thermal resistance model. The thermal resistance of a heat pipe is given as

$$R_{th} = \frac{T_{eva} - T_{cond}}{\dot{Q}}$$

(Eqn 1.1)

where T_{eva} is the evaporator temperature, T_{cond} is the condenser temperature and $\dot{Q}$ is the heat flux. The thermal resistance of the heat pipe is a function of heat flux and the inclination of the heat pipe.

Heat pipes are also characterized by heat transfer limits such as capillary limitation, sonic limitation, viscous limitation, and entrainment limitation. At low temperatures, the maximum heat transfer is determined by viscous forces rather than inertial forces because of low vapor pressure and density, known as the viscous limit. During high temperatures, the fluid starts to flow with higher velocity, and at a certain point, the fluid rate reaches the speed of sound. After this, no further increase in fluid rate can be obtained, and this limit is considered the sonic limitation. In the working stage, the entrainment limit appears if the vapor velocity is high, and the pressure is low. In such cases, some bubbles might be carried back to the condenser section by vapor flow [6].

The capillary pressure in the heat pipe is the main reason for the liquid in the condenser to flow back to the evaporator. This flow from condenser to evaporator consists of several pressure drops. The maximum capillary pressure in the heat pipe shall be higher than the sum of all the pressure drops, so that the fluid flows back to the evaporator and avoids evaporator burnout [8]. This capillary limitation is expressed as

$$\Delta P_{c,max} \geq \Delta P_{tot}$$

(Eqn 1.2)

The total pressure drop (ΔP_{tot}) in the heat pipe is given as sum of the friction pressure drop in vapor and liquid paths, pressure drop due to body force (e.g., gravity, centrifugal, electromagnetic) and the pressure drop due to phase change

$$\Delta P_{tot} = \Delta P_v + \Delta P_l + \Delta P_b + \Delta P_{ph}$$

(Eqn 1.3)

Patrik et al. [8] developed a mathematical model to determine the effect of heat transfer limits on heat pipes. They found that these limits depend upon the wick structure, heat pipe structure, working medium filling volume and inclination. At lower temperatures near the freezing point of the working fluid, the viscous limitation effects the performance of the heat pipe. The critical effect during the normal working pressure on the performance was due to the entrainment limitation, and capillary limitation.

1.2.2 Bubble Pump Model

The vapor absorption refrigerant cycle is primarily driven by heat energy but requires mechanical energy to circulate the refrigerant-absorbent solution from absorber to reservoir. Platen and Munters [9] used the bubble pump technique with two phase fluids to generate this mechanical energy without the need for any mechanical pumps. Figure 1-5 shows the schematic of the bubble pump used in the vapor absorption cycle. The bubble pump is a long tube with length (L) and diameter (D) that uses the heat supplied to it to boil the working fluid. The vapor bubbles generated raise high in the tube and reaches the reservoir. The two-phase fluid is then cooled and sent back to the absorber [10].

With no moving parts, silent operation and portability, the vapor absorption cycles with bubble pump are highly reliable. The bubble pump performance is determined by the circulation ratio, the ratio of mass flow rate of fluid leaving the bubble pump to the mass flow rate of the fluid entering it. One of the biggest disadvantages of these systems is the low cooling capacities [10].

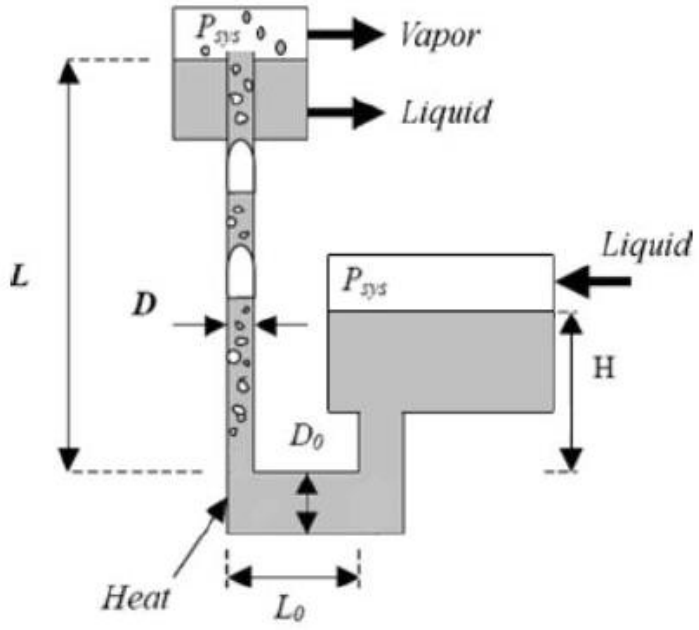

Figure 1-5: Schematic of bubble pump model for Vapor absorption cycle [10]

Benhmidene et al.[11] used two-phase fluid models to investigate the influence of heat supplied to the bubble pump at different conditions on its performance. It was proposed that the optimum heat input is a function of the bubble pump tube diameter and mass flow rate, while the minimum heat input is a function of only the tube diameter. Ben Ezzineet et al.[12] conducted experimental investigation on air-cooled diffusion-absorption refrigeration machine with a boiler and bubble pump varying the heat input from 170W to 350W. They observed that the Coefficient of Performance (COP) of the machine reached a maximum of 0.14 with these conditions.

1.2.3 Self-propelling bubbles using surface asymmetry

Linke et al. [13] reported that in the Leidenfrost regime, bubbles exhibit self-propelled motion when placed over a heated ratchet-like asymmetric surface topology. It was proposed that the steady-state preferential droplet motion is a result of the balance between curvature difference in the bottom surface of the liquid droplet between the crest and trough of the ratchets, and viscous forces exerted by vapor flow between

the bubble and the surface, as illustrated in Fig. 1-6. They observed that a millimeter-sized droplet can accelerate at rates of 1 – 2 m/s², climb inclines, and sustain speeds of 5 cm/s up to a distance of 1 meter.

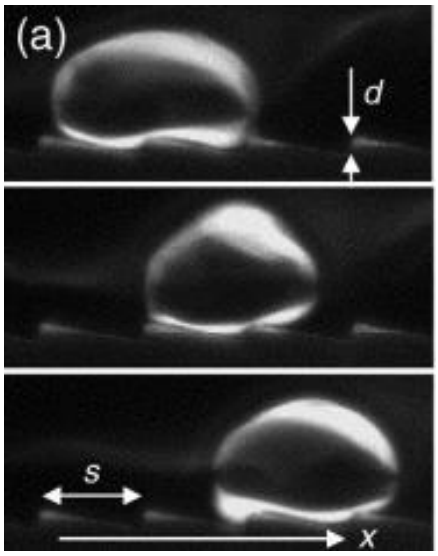

Figure 1-6: (a) Self-propelled motion of a R134a droplet on horizontally leveled, brass surface with ratchetlike topology (d 0:3 mm, s 1:5 mm) [13]

The study by Linke et al. [13] revealed that self-propelling bubbles can be obtained in the Leidenfrost regime. However, in the Leidenfrost regime the heat transfer rates are poor, and the surface temperatures are very high for the practical engineering devices. Kapsenberg and Thiagarajan [14] employed the concept of surface asymmetry in microstructure to induce lateral motion in the fluid within the nucleate boiling regime, where the heat transfer rates are higher with lower surface temperatures. They used asymmetry on the surface in the form of 30-60^0 ratchets with reentrant cavities added on 30^0 faces and observed that the growing bubble on the ratchet has resulted in a liquid mean velocity of 25 mm/s parallel to the surface as illustrated in the figure 1-7(a). With no moving parts, this concept can provide for an innovative means of heat transfer and mass transport of the two-phase fluid.

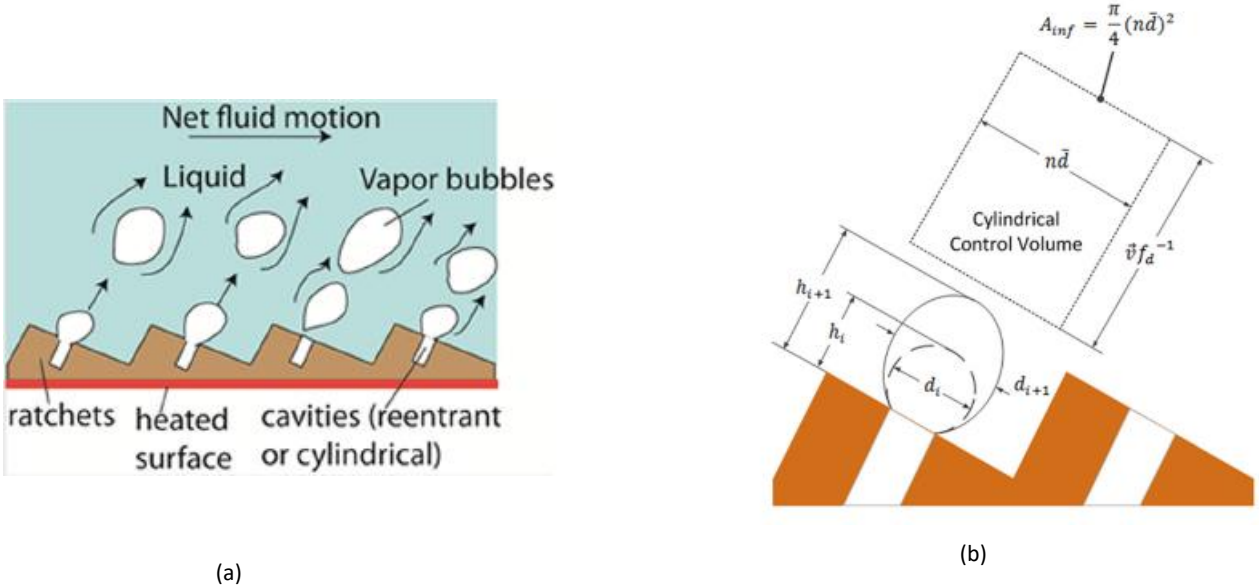

(a) (b)

Figure 1-7: Bubble growth on the asymmetric surface (a) Schematic of bubble pumping technique in nucleate boiling regime (b) Model for bubble growth and the affected surrounding control volume [14]

With the bubble growth data obtained from the experiment, they developed a semi-empirical model to calculate the velocity generated by a growing bubble on the ratchet to the surrounding fluid. A momentum balance was applied between the bubble growing on the ratchet and the surrounding fluid in the affected control volume, as shown in figure 1-7(b). The time rate of change of momentum from the bubble was equated with the drag force overcome by the growing bubble during each cycle.

Consider a bubble of diameter d_i and height of h_i at a time instant is growing on the ratchet surface as shown in figure 1-7(b). After some time, the bubble diameter increased to d_{i+1} and height to h_{i+1}. This growth of bubble imparts a momentum to the surrounding fluid in the affected control volume (as shown in fig. 1-6b). The control volume is considered to be cylindrical with a diameter equal to multiplying factor (n) times the average bubble diameter of the bubble in given time. The cross-section area of this cylindrical control volume was the area of influence of the bubble and represented as $A_{inf.}$ The momentum transferred by the growing bubble to the surrounding fluid is given by:

$$P_l = m_{f\_inf}\overline{v}_l$$

(Eqn 1.4)

$$P_l = \{\rho_l A_{inf}\overline{v}_l f_d^{-1}\}\overline{v}_l$$

(Eqn 1.5)

Where P_l is the momentum on the surrounding liquid, m_{f_inf} is the mass of fluid in the control volume, v_l is the velocity imparted by growing bubble and ρ_l is the density of the fluid. The volume of surrounding fluid in the affected control volume is given by the cross-section area of A_{inf} and the height of control volume given by velocity (v_l) times the inverse of frequency of departure of bubble (f_d^{-1}). A force balance between this momentum transfer and the drag force (F_g) on a growing bubble in a given time (t) is given by:

$$F_g = \frac{dP_l}{dt} = \frac{d\{\rho_l A_{inf}\overline{v}_l f_d^{-1}\}\overline{v}_l}{dt}$$

(Eqn 1.6)

Drag force on the bubble can be calculated as

$$F_g = \frac{1}{2}\{\rho_l C_d A_b v_b\}v_b$$

(Eqn 1.7)

Where ρ_l is the density of the fluid, C_d is the drag coefficient, A_b is the area of cross section of bubble of diameter (d) and v_b is the velocity of growing bubble. The velocity of the growing bubble was given by change in height of bubble (h) in a given time (t). Therefore,

$$F_g = \frac{\pi}{8}\rho_l C_d d^2\left\{\frac{\partial h}{dt}\right\}^2$$

(Eqn 1.8)

Comparing the momentum and the drag force (equation 1.6 and 1.8) can provide an average velocity of liquid in the control volume.

$$\overline{v_l} = \sqrt{\frac{\pi f_d}{8A_{inf}} \sum_{i=\,t_0+1}^{t_f} \overline{C_D} \left(\frac{d_i + d_{i-1}}{2}\right)^2 \left(\frac{h_i - h_{i-1}}{dt}\right)^2 dt} \qquad \text{(Eqn 1.9)}$$

The frequency of departure can be replaced by 1/dt to obtain the average velocity in each time frame. Thus, the average velocity of fluid imparted by a growing bubble in each time can be given by

$$\overline{v_l} = \sqrt{\frac{\pi}{8A_{inf}} \sum_{i=\,t_0+1}^{t_f} \overline{C_D} \left(\frac{d_i + d_{i-1}}{2}\right)^2 \left(\frac{h_i - h_{i-1}}{dt}\right)^2} \qquad \text{(Eqn 1.10)}$$

In his research, Strid [15] found that as the area of influence decreased, the velocity predicted by the empirical formula showed fewer discrepancies. He recommended an area of influence equal to the cross-sectional area of a cylinder with diameter equal to average diameter of bubble(d) multiplied with a factor of n=1.

$$A_{inf} = \frac{\pi}{4} \left(n\bar{d}\right)^2 \qquad \text{(Eqn 1.11)}$$

In microgravity environments, the absence of buoyancy causes bubbles generated from two-phase heat transfer to stagnate over the heated electronics surface, elevating local temperatures beyond the operating limits. While the use of pumps in flow boiling can dissipate higher heat fluxes, it introduces complexity to the design and increases weight [16].

Studies indicate that in microgravity, larger vapor bubbles tend to form, leading to poor heat transfer. In a drop tower experiment, Xue et al. [17] observed two distinct modes of bubble growth and departure in a microgravity environment. At low wall superheats, larger bubbles grew on the surface with no coalescence. As the heat flux increased, more bubbles ebulliated and merged to form a larger-diameter

bubble, eventually departing from the surface. The passive motion of fluid, facilitated by surface asymmetry could prove beneficial in replacing the buoyancy force and assisting in the departure of bubbles from the surface in the microgravity.

A parabolic flight experiment conducted by Thiagarajan et al. [18] utilized a microstructure surface with a sawtooth profile. It was observed that FC-72 vapor bubbles generated in microgravity were larger compared to the terrestrial environment, sliding across the surface with velocities of up to 27.4 mm/s. Building on this, Bhavnani et al. [19] proposed a slug transport model, suggesting that the sliding of vapor bubbles over the microstructure surface resembles a fully developed planar Couette-Poiseuille flow. The driving force for slug motion is considered to be the pressure difference between the crest and the trough of the sawtooth, resulting in a net pressure gradient in the direction of the long slope.

Sridhar et al. [16] conducted terrestrial experiments with the downward facing sawtooth profile surfaces in the nucleate boiling regime to replicate the microgravity environment. A force balance for the slug transport model proposed by Bhavani et al. was conducted leading to a semi empirical formula. The original high-speed image obtained from the experiment and the proposed schematic of slug flow are illustrated in figure 1-8.

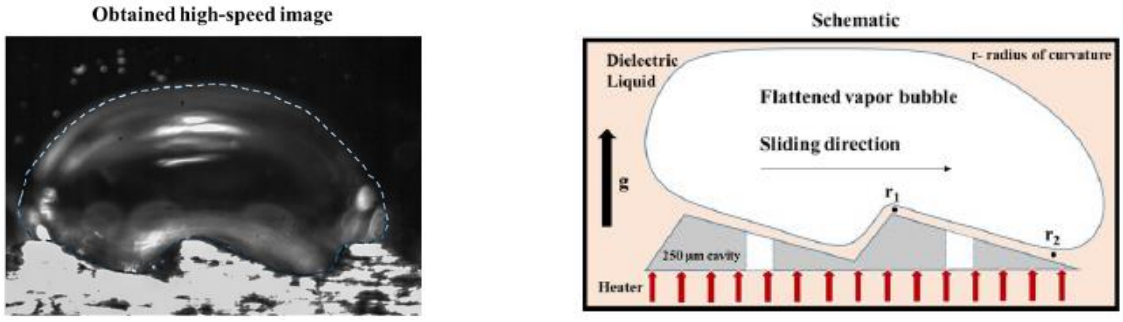

Figure 1-8: Slug transport model (a) Original image from experiment (b) Schematic proposed. [16]

The pressure drop along the saw tooth was expressed using the Young-Laplace equation with the radius of curvature at crest (r_1) and trough (r_2), pressures $P_{1,l}$ at crest and $P_{2,l}$ at trough and surface tension of fluid (σ).

$$P_{1,l} - P_{2,l} = 2\sigma\left(\frac{1}{r_1} + \frac{1}{r_2}\right)$$

(Eqn 1.12)

The horizontal component of the shear force acting on the vapor bubble sliding on the microstructure with a velocity V is calculated using the Couette-Poiseuille flow and is given as

$$F_{\Delta P,tot} = \begin{Bmatrix} m\left[\left(\frac{\mu V}{H} + \frac{H}{2}\frac{\partial P}{\partial x}\right) LW\cos\theta\right]_{long\ slope} \\ -n\left[\left(\frac{\mu V}{H} + \frac{H}{2}\frac{\partial P}{\partial x}\right) LW\sin\theta\right]_{short\ slope} \end{Bmatrix}$$

(Eqn 1.13)

where $\frac{\partial P}{\partial x}$ is the pressure gradient between the crest and trough, H is the liquid film thickness formed between the surface and the vapor bubble, θ is the angle of saw tooth, L is the length of the liquid film, W is the equivalent diameter of vapor bubble, μ is the dynamic viscosity of fluid, m and n are the number of long slopes and short slopes covered by the vapor slug respectively.

As the vapor bubble slides over the surface, the drag force (F_d) acts against the bubble and is expressed as

$$F_d = 4\pi\mu RV$$

(Eqn 1.14)

Where R is the equivalent radius of the bubble (R = W/2)

While the momentum transfer from the growing bubble on the ratchet is negligible in microgravity, a major contribution of force is generated from the kinetic energy resulted from the coalescence of the bubbles, which is given as

$$F_v = \pi \sum_{i=1}^{k} \mathrm{D}_\mathrm{i}^{\frac{5}{2}} \overline{f_i} \sqrt{(\frac{\sigma_i \rho_{v,i}}{3})}$$

(Eqn 1.15)

where f_i is the mean bubble departure frequency, D_i is the bubble departure diameter.

The total force balance for this model can be represented as:

$$F_{\Delta P,tot} + F_v - F_d = 0$$

(Eqn 1.16)

Using this force balance, and by determining radii and vapor thickness from the high-speed images, the velocity of the vapor slug can be determined. Sridhar [16], using this force balance in his experiments predicted that the slug moving with a velocity of 13.7 mm/s at heat flux input of 1.25 W/cm^2 will slide on a 49 µm liquid film.

For over a century, researchers have developed extensive experimental methods and proposed various models and empirical equations for bubble transport. However, these experiments are often narrowly restricted to specific conditions that are challenging to replicate, necessitating rigorous validation. One approach to validate these models is to analyze the thousands of images obtained from experiments, focusing on bubble and slug properties. Nevertheless, the complexity of nucleation statistics, bubble growth, coalescence, departures, and slug development make it challenging to detect and track each moving object within the frame [20].

To analyze information-rich imagery commonly obtained from phase change heat transfer experiments, advanced image processing techniques are essential. Computer vision algorithms with thresholding and

edge detection are popular in this type of analysis. However, these techniques are highly dependent on the experimental environment, such as lighting and contrast, leaving room for the development of machine learning and deep learning techniques. The main goal of the thesis is to develop advanced Image Processing and Particle tracking velocimetry (PTV) algorithms to analyze the two-phase flow imagery data obtained from the experiments to validate the bubble pumping model proposed by Kapsenberg [14] in the nucleate boiling regime.

1.3 Scope

A review of the literature in section 1.2 has revealed that the asymmetric surface and the reentrant cavities could possibly provide a passive lateral motion in the fluid. Higher heat fluxes from phase change heat transfer, and passive thermal pumping in nucleate boiling regime can greatly benefit thermal management of electronics in space, immersion cooling techniques, and passive thermal management techniques. Two different mechanisms have been identified for the thermally actuated pumping using ratcheted surfaces in prior studies – (1) a bubble pump model developed by Kapsenberg et al. [14], which attributes the lateral motion to the momentum imparted by the growing bubble to the surrounding liquid, and (2) asymmetry in the curvature of the slug that spans several ratchet lengths, resulting in a net surface tension force along the 30-degree slope of the ratchet [19]. The work done by Kapsenberg et al. [14] confirms that the momentum transfer by the growing bubble on the ratchet in the nucleate boiling regime results in the surrounding liquid mean velocities of around 25 mm/s to 70 mm/s parallel to the surface. Kapsenberg et al.'s experiments were performed with a horizontal, upward facing ratchet in a pool of liquid. The work discussed in this thesis will focus on the validation of this bubble pumping mechanism and the semi-empirical formula developed by Kapsenberg et al. for vertically oriented ratchets in a mm-scale channel. A channel is created for this purpose using the asymmetric ratchet surfaces with four nucleation sites in each vertical wall such that each site can potentially provide thermally actuated bubble pumping in the same preferential direction in the nucleating boiling regime.

1.4 Objectives and Tasks

The thesis provides verification for the concept that the bubble growing on the asymmetric ratchet provides lateral motion to the surrounding fluid in a preferential direction. The semi-empirical formula (Eqn. 1.10) developed by Kapsenberg [14] for the calculation of velocity imparted by the growing bubble will also be validated.

The validation is performed by image analysis on recent experiments conducted by Safarkoolan et al. [21]. The ratchet test sections were designed and fabricated using wire electric discharge machining (EDM) method. Four “hammer-shaped” reentrant slots were located on the shallow slope of each 1.5-mm ratchet. Using serpentine heaters on the test section, heat flux was imparted and thus the bubbles are grown at the nucleation sites. The test facility included current and voltage measurement and control, pressure measurement and control, pool temperature measurement and fluid sub cooling control, and the ability to visualize the bubble growth using high speed videography. The test was conducted for five different heat flux and the subcooling conditions for the validation of bubble pumping in the whole nucleating boiling regime. One more condition of reversing the nucleation site direction was conducted to confirm that the bubble growth on ratchet surface facilitates fluid motion in a preferential direction.

In this thesis, image processing techniques were used to analyze the bubble growth on the ratchet by quantifying the bubble height and diameter in each frame. This data, along with the semi-empirical model from Kapsenberg et al. [14] is used to calculate the velocity imparted by the growing bubble. High speed videography also captures the smaller bubbles in the flow, whose velocity is indicative of the liquid velocity. This velocity was estimated using bubble tracking velocimetry. The velocities obtained from the semi-empirical model and the bubble tracking velocimetry were compared to assess whether the bubble pumping model can explain the thermally driven lateral motion observed in the experiments.

CHAPTER 2 EXPERIMENTAL FACILITY AND PROCEDURE

This section covers the detailed description of the entire experimental facility used to validate the concept of bubble pumping in the nucleate boiling regime as proposed by Kapsenberg [14]. Safarkoolan et. al. [21] developed the complete facility and conducted experiments, resulting in the high-speed imagery for six different cases of subcooling and heat fluxes. This chapter discusses the complete details of the ratchet test section, test chamber and the procedures followed during the experiment. All these tests were conducted with the dielectric fluid FC-72.

2.1 Test section

The test section consists of a structured ratcheted surface on a grade 5 titanium substrate, as shown in figure 2-1, fabricated using wire electric discharge machining (EDM). Two types of asymmetries were introduced in the test section – a) ratchets with 30–60-degree slope on the surface with a pitch of 1.5 mm, and b) reentrant cavities in every third ratchet on the shallow slope. The crests and troughs of the ratchet were rounded to prevent stray nucleation sites at these locations. Additionally, two notches, each of 250 µm wide and 1.5 mm deep, were designed on the heated side of ratchet to mitigate axial heat conduction.

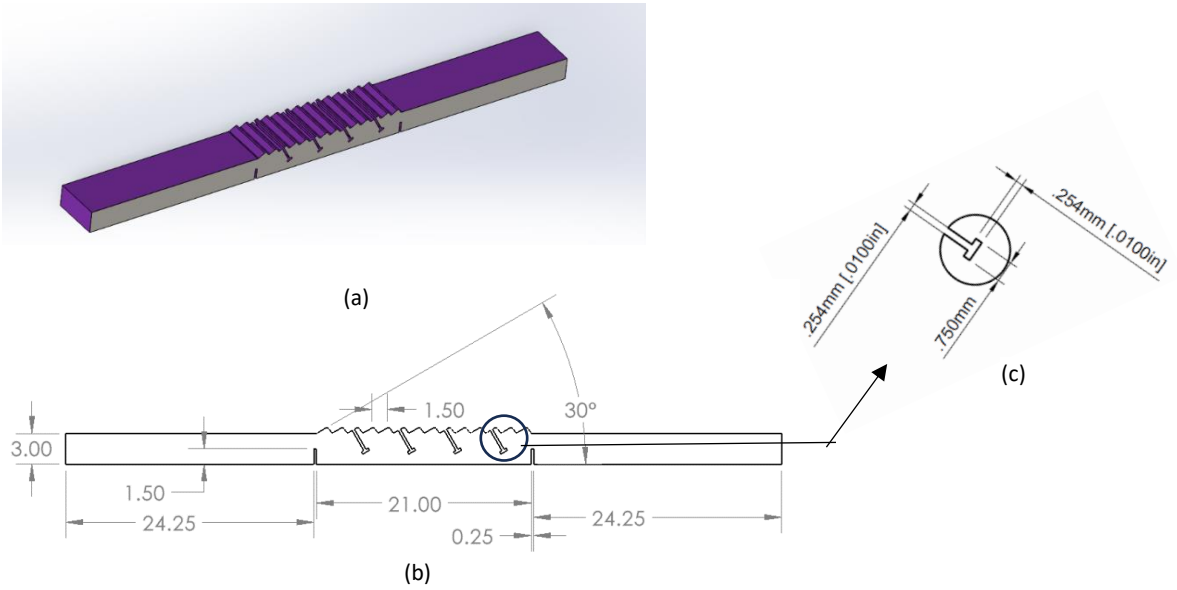

Figure 2-1: Fabricated ratchet test section (a) Isometric view (b) Dimensions of the test section (c) Dimensions of the nucleation site. All dimensions in mm

A channel was created by placing two ratchets vertically opposite to each other. Figure 2-2 shows an exploded view of this open-ended channel. The top and bottom walls of the channel were made of transparent polycarbonate and spanned the whole ratchet length of 70 mm. Thick-film heaters, 18 mm in length and 4 mm in depth, were located on the backside of the ratchet test section and located in between the two notches. Each heater was composed of a 0.254 mm thick steel serpentine shim, sealed within Kapton tape, and insulated with high-temperature Ultem™ plastic on the backside. Controlling the voltage applied to the serpentine heaters enabled precise control of the heat flux through the titanium ratchet.

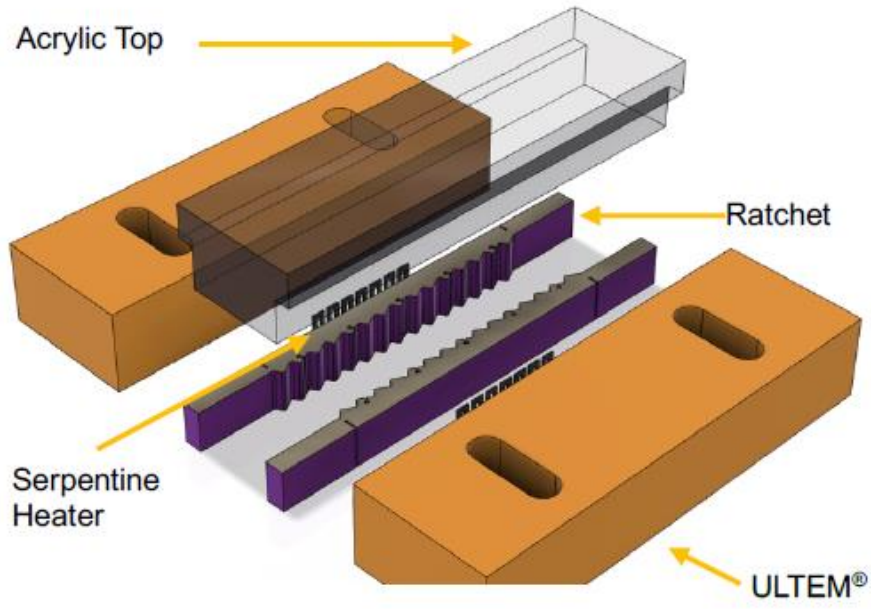

Figure 2-2: Exploded view of the open-ended channel [21]

2.2 Test Chamber

The test chamber, as shown in figure 2-3, consisted of a transparent polycarbonate base and top with an aluminum chamber sandwiched between them. Thermocouples and a pressure transducer were inserted inside the polycarbonate lid to measure the pool and vapor temperatures and the pressure inside the chamber. Two opening ports with valves were provided on the lid. One was used to fill the chamber with the test fluid FC-72 fluid and also to open the chamber to atmospheric pressure, while the other served as a connection for vacuum pump to degas the fluid.

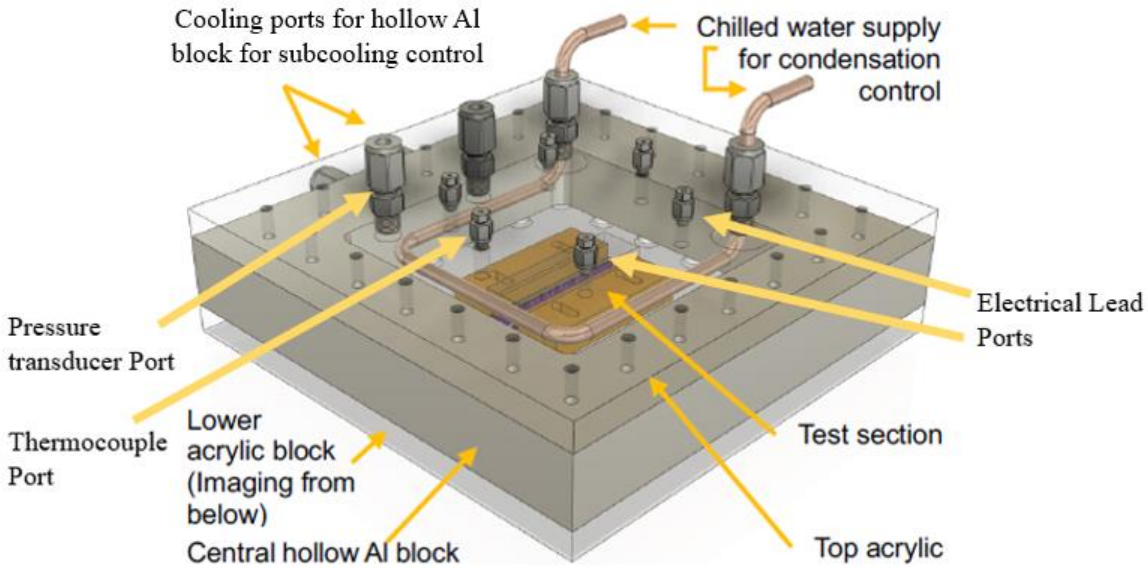

Figure 2-3: Exploded view of the test chamber [21]

The aluminum chamber sidewalls were equipped with internal fluidic passages exposed to both the pool and vapor within the chamber, allowing the regulation of pool temperature, vapor temperature, and chamber pressure through condensation. To enhance more control over condensation, a copper pipe loop,

as depicted in Figure 2-3, was incorporated. Thermocouples were employed to measure the outlet water temperatures of both the aluminum block and the copper tube. Achieving the desired subcooling values at stable chamber pressures involved the coordinated adjustment of the temperature in the aluminum fluidic loop and the flow rate in the copper condensation loop using a gear pump. Figure 2-4 illustrates the outer cooling loops used to maintain the chamber conditions. The recirculating water chiller was used for the aluminum fluidic passages, and cold water from the storage reservoir in the lab was used for the copper condensation control loop.

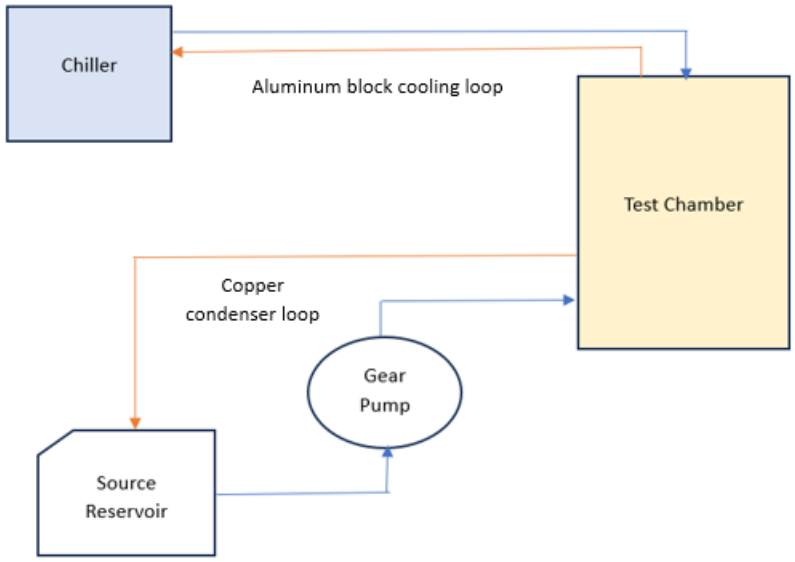

Figure 2-4: Layout of the cooling loops used for maintaining chamber conditions (Red and blue indicates hot and cold lines respectively)

Electrical connections to the heater were established through the electrical lead ports available on the top transparent lid. Voltage and current were controlled using a regulated DC power supply. The assembly process involved the separate positioning of ratchets, heaters, and the Ultem insulating block at the center of the chamber. To align the walls parallel to each other, a transparent precision polycarbonate block was used. After securing the walls to the chamber, a polycarbonate piece was used as an upper wall, spanning

the gap between the two vertical walls. Dielectric fluid FC-72 was introduced into the chamber through the port on the top lid by creating sub-atmospheric pressure in the chamber using a vacuum pump. Notably, the cold-water passages in the aluminum block-maintained contact with the pool and vapor, while the copper condensation loop exclusively interacted with the vapor. Post-assembly, when viewed from the front, the channel had dimensions of a height equivalent to the thickness of the heated ratchets (6.35 mm) and a width of 9 mm.

2.3 Test Facility

The test facility consisted of the chamber placed on four legs. A 45-degree mirror was positioned at the bottom, and a custom-designed LED array was provided on the top of the chamber for backlighting. A high-resolution camera was employed to focus on the channel through the mirror and capture the flow using the optical shadowgraph method as shown in figure 2-5. The aperture, shutter speed, and frame rate were adjusted using the Photron FASTCAM Viewer (PFV) application to focus on the required region. The temperatures and pressure readings were recorded using a National Instruments data acquisition system (DAQ). Experiments were conducted for six different cases of subcooling, and heat flux as shown in table 2-1. The complete experiment was recorded at 4000 fps for approximately 5 seconds, providing 21,000 frames for each case for analysis.

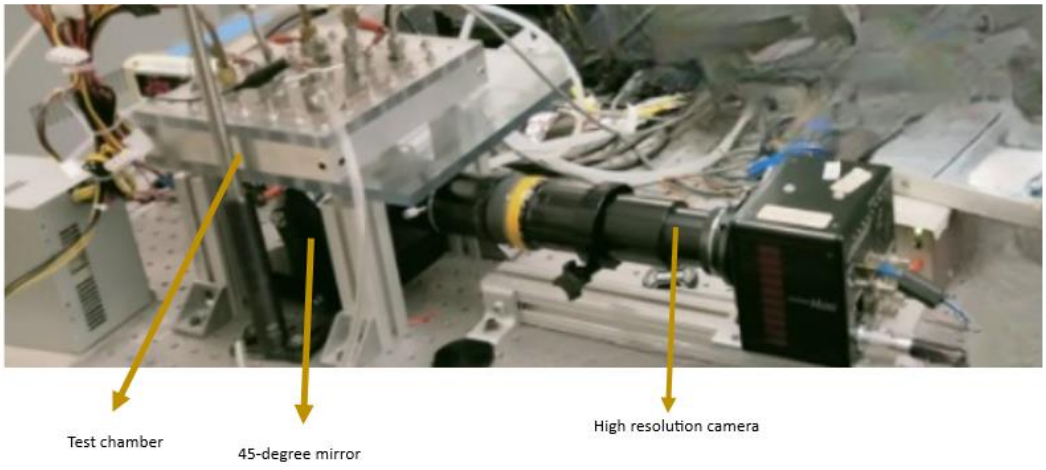

Figure 2-5: High resolution camera used to capture the flow.

Table 2-1: Summary of various Subcooling and Heat Flux test conditions

S.No.	Condition	Conditions on each ratchet				Average Power, W	Surface area, cm2	Heat flux, W/cm 2	Sub cooling [^{0}C]
		Voltage, V	Current, Amp	Voltage, V	Current, Amp				
1	High Subcooling High Heat Flux - HSHH	1.01	3.1	0.96	3.1	3.05	1.24	2.47	10.52
2	High Subcooling High Heat Fux Reverse - HSHHR	1	3.2	1	3.3	3.25	1.24	2.62	9.65
3	High Subcooling Mid Heat Flux - HSMH	0.76	2.3	0.75	2.3	1.74	1.24	1.40	10.8
4	Mid Subcooling Mid Heat Flux - MSMH	0.77	2.4	0.76	2.4	1.84	1.24	1.48	5.7
5	Low Subcooling Mid Heat Flux - LSMH	0.76	2.2	0.74	2.2	1.65	1.24	1.33	2.76
6	Low Subcooling Low Heat Flux - LSLH	0.59	1.8	0.6	1.8	1.07	1.24	0.86	2.3

2.4 Experimental Procedure

The chamber was filled with the dielectric fluid FC-72, and a vacuum pump was used to remove air from the chamber and degas the liquid. To mitigate the influence of gravity on the experiment, the test chamber was leveled by conducting a standing bubble test. A bubble was nucleated on the test section by supplying power to the electrical heaters. Once the bubble began departing from the nucleation site, power to the

heaters was promptly turned off. The legs supporting the test chamber were adjusted until the bubble remained stationary for at least two minutes. This leveling process was repeated after rotating the chamber 180 degrees to ensure that gravity had no effects.

Preliminary experiments were carried out to determine safe subcooling and heat flux ranges for the experiment without causing surface burnout. These ranges were established to ensure bubble nucleation at high subcooling and the visibility of constant slugs at lower subcooling. Subcooling was achieved by controlling the temperature of the fluid loop in the aluminum block using recirculation chillers. If still the desired subcooling was not attained, the copper condensation loop was used to maintain the chamber pressure. Once the subcooling and heat flux conditions were finalized, the actual experiment proceeded by providing the necessary power to the heaters and maintaining the required subcooling for each case. High-speed images for all the cases were captured in the form of TIFF files, which were subsequently post-processed to obtain the required data.

CHAPTER 3 DATA ANALYSIS

This chapter covers Image processing and the data analysis of the high-speed videos obtained from the experiments discussed in the previous chapter. The bubble growth on the ratchet surface was analyzed using image processing in MATLAB for all conditions of heat flux and subcooling in the experimental matrix. Using this data, the velocity imparted by the growing bubble on the ratchet to the surrounding fluid was obtained from the empirical formula introduced by Kapsenberg et al. [14]. This velocity was compared with the mean velocity of the fluid obtained by tracking the smaller diameter bubbles available in the flow using Particle (Bubble) Tracking Velocimetry (PTV) techniques. A detailed description of image processing of the attached bubbles, PTV of the small-detached bubbles in flow, and uncertainty analysis are discussed in this chapter.

3.1 Velocity Comparison

To validate the concept of bubble pumping and the semi empirical formula, the horizontal velocity generated by a growing bubble in the surrounding fluid calculated using the semi empirical formula was compared with the horizontal mean velocity of the flow obtained from PTV. The velocity imparted by the growing bubble to the surrounding fluid was given by equation 1.10 in the Chapter 1. The same equation is provided again below for ease of understanding.

$$\overline{v_l} = \sqrt{\frac{\pi}{8A_{inf}} \sum_{i=t_0+1}^{t_f} \overline{C_D} \left(\frac{d_i + d_{i-1}}{2}\right)^2 \left(\frac{h_i - h_{i-1}}{dt}\right)^2} \qquad \text{(Eqn 3.1)}$$

However, this velocity obtained from the semi-empirical formula was constrained to the 'Area of Influence,' as discussed in the chapter 1, while the mean velocity of flow from PTV was calculated for the

entire ratchet area. To make these velocities comparable, a momentum balance was conducted. Figure 3-1 shows the area considered for calculation of both the velocities.

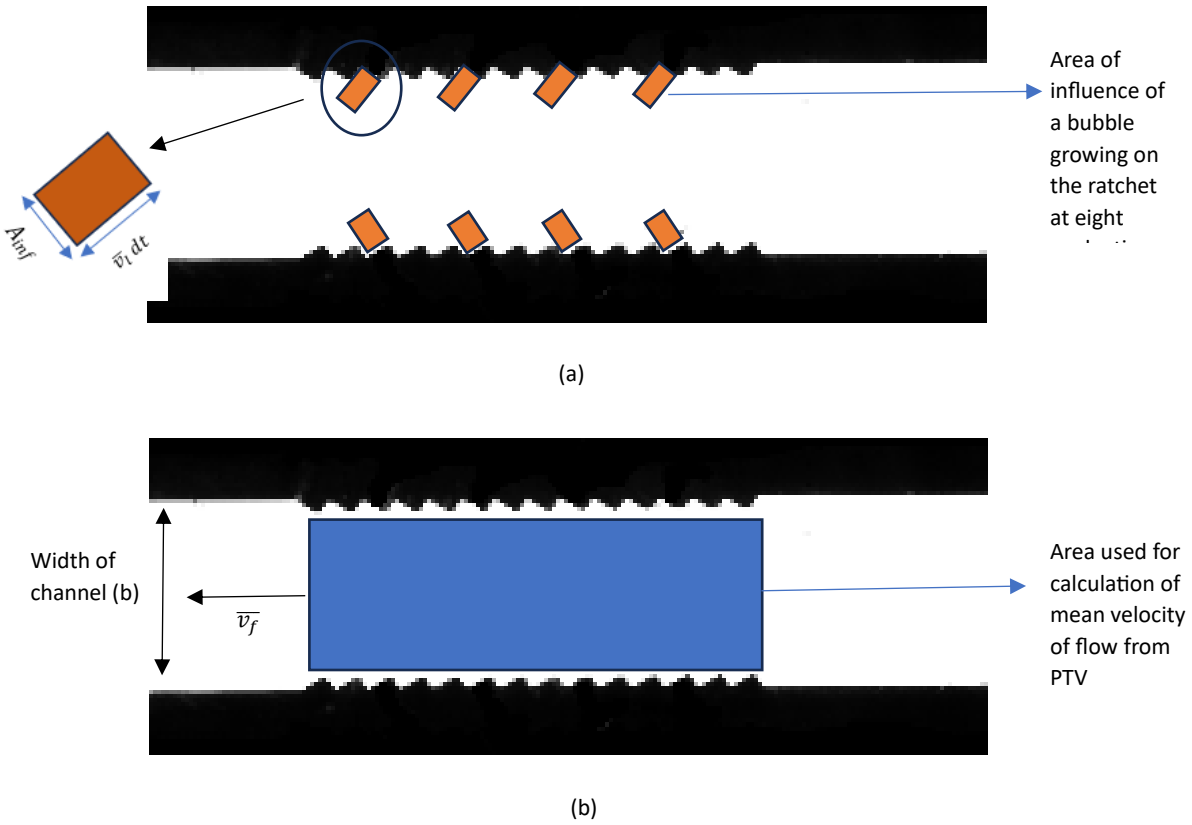

Figure 3-1: Area considered for velocity calculation (a) Area of influence of each bubble on nucleation site (b) Area of ratchet considered for mean velocity calculation (PTV)

The momentum of fluid in the channel is equal to the sum of momentum generated by growing bubbles on ratchet in the surrounding fluid.

$$m_{f\_c}\,\overline{v_f} = \sum_{k=1}^{8} m_{f\_inf}\,\overline{v_l}$$

(Eqn 3.2)

Where m_{f_c} and v_f are the mass and velocity of fluid in the channel, m_{f_inf} is the mass of fluid in area of influence region of bubble growing on the ratchet and v_l is the velocity in the surrounding fluid imparted

by growing bubble calculated by the semi empirical formula (eqn. 1.10). Total momentum imparted by all the growing bubbles at eight nucleation sites (k = 1 to 8) was equated to momentum of fluid in the channel.

Mass of fluid was calculated using the following relations.

$$\text{Mass of fluid} = \text{Density of fluid} * \text{Volume of fluid displaced}$$

$$\text{Volume of fluid diplaced} = (\text{Area of cross section of influence region}) * \text{height of the influence region}$$

$$\text{height of the influence region} = \text{Velocity} * \text{time}$$

Therefore,

$$m_{f\_c} = \rho_f * (b\ d\ \overline{v_f}\ dt)$$

(Eqn 3.3)

$$m_{f\_inf} = \rho_f * (A_{inf}\ \overline{v_l}\ dt)$$

(Eqn 3.4)

where b and d are width and depth of channel respectively, ρ_f is the density of fluid and A_{inf} is the area of influence of the growing bubble on ratchet and dt is the time. From equation 3.2,3.3 and 3.4:

$$(\rho_f\ b\ d\ \overline{v_f}\ dt)\overline{v_f} = \sum_{k=1}^{8} (\rho_f\ A_{inf}\ \overline{v_l}\ dt)\ \overline{v_l}$$

(Eqn 3.5)

$$b\ d\ (\overline{v_f}^2) = \sum_{k=1}^{8} A_{inf}\ (\overline{v_l}^2)$$

(Eqn 3.6)

$$\overline{v_f} = \sum_{k=1}^{8} \sqrt{\frac{A_{inf}}{bd}}\ \overline{v_l}$$

(Eqn 3.7)

As we were interested in understanding the lateral motion induced by the growing bubble, the horizontal components of velocities were compared.

$$v_{f\_h} = \sum_{k=1}^{8} \sqrt{\frac{A_{inf}}{bd}}\ v_{l\_h}$$

(Eqn 3.8)

v_{f_h} and v_{l_h} are the horizontal components of mean flow velocity of the flow and the velocity obtained from the semi empirical formula respectively.

This correlation was used to compare the horizontal velocity generated by the growing bubble in the surrounding fluid calculated from semi empirical formula and the mean velocity of the flow obtained from PTV. To calculate the velocity obtained from the semi empirical formula, the height and diameter values of the bubble attached to the ratchet were needed. For mean flow velocity, the bubbles in the flow were to be detected, and tracked. Image processing and the PTV techniques were used to extract this data from the high-speed images. Figure 3-2 shows a brief overview of this approach used for data analysis.

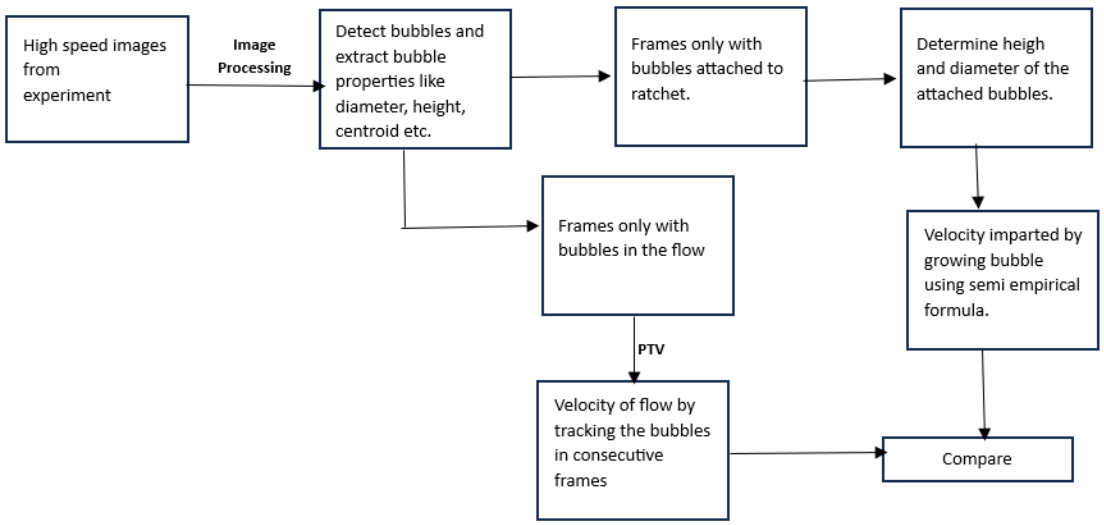

Figure 3-2: Schematic of the approach used for data analysis

3.2 Bubble growth image processing methodology

The high-speed videos were captured at a frame rate of 4000 fps for various heat flux and subcooling conditions such that each condition has around 21,000 frames for analysis. The main objective of the image processing was to analyze each frame by identifying the bubbles that were attached to the ratchet at each nucleation site and determine the height and diameter of these attached bubbles. Image processing was conducted in MATLAB.

3.2.1 Identifying Bubbles attached to ratchet

A series of Image processing techniques were applied to determine the bubbles that were attached to the ratchet at nucleation sites. The original frames, obtained from the high-speed video in the form of Tiff files, were imported into Matlab. The ratchet in each frame was removed using a background image developed by Z projection in ImageJ software, resulting in an image showing only bubbles, as illustrated in figure 3-3.

(a) (b) (c)

Figure 3-3: Image Processing Background deletion. (a) Original Tiff image (b) Background image developed by Z projection in ImageJ (c) Resulting background-subtracted image

The resulting image's histogram was adjusted over the entire grayscale using "imadjust" to achieve maximum contrast without losing any data. The images were then binarized to convert them into bi-level images. These binarized images were inverted such that the bubbles were represented as bright objects in a black background. Any pixels with values less than 50 were deleted to reduce noise. Pixel coordinate system, where the image was treated as a grid of discrete elements, ordered from top to bottom and left to right, as shown in figure 3-4 was used to specify the locations in the image. Any location in the image was specified using pixel coordinates, which are any integer ranging from 1 to length of columns or rows of the grid.

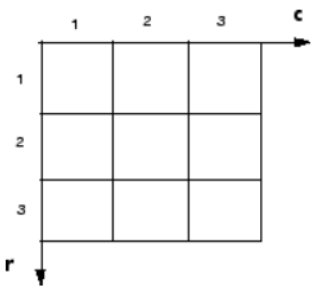

Figure 3-4: Schematic of pixel coordinate system. Origin is at top right of the image.

Bubbles with centroid x-coordinate less than 220 pixels (15 mm from left of the ratchet) were removed to ensure that only bubbles in the ratchet area were considered for analysis. To determine the geometric properties of the bubble such as centroid, diameter etc., the first step was to detect the location and the boundaries of the bubbles in the image using edge detection and segmentation techniques. Active contour and water shed techniques in MATLAB were used for the edge detection and segmentation. The image obtained after removing the bubbles away from the ratchet area was segmented using the initial original image as a mask through active contouring. This resulted image created the boundaries for all the bubbles present in the image. Subsequently, the holes present in the image were flood filled with the “imfill” command. Some of the bubbles in the image were located very close to each other spatially, such that the “active contour” command merged these bubbles. To ensure proper segmentation, the water shed technique with distance transform was applied.

After applying edge detection and segmentation techniques, the image was reevaluated for any non-closed objects using solidity. Solidity is defined as the ratio of area of the object to its convex hull (a completely closed form). The solidity of the bubble was used to identify unclosed bubbles, and a convex hull operation was applied only to close these bubbles in the image, ensuring a proper segmentation and closure of each bubble in the frame. Figure 3-5 displays example images at each step of the image processing.

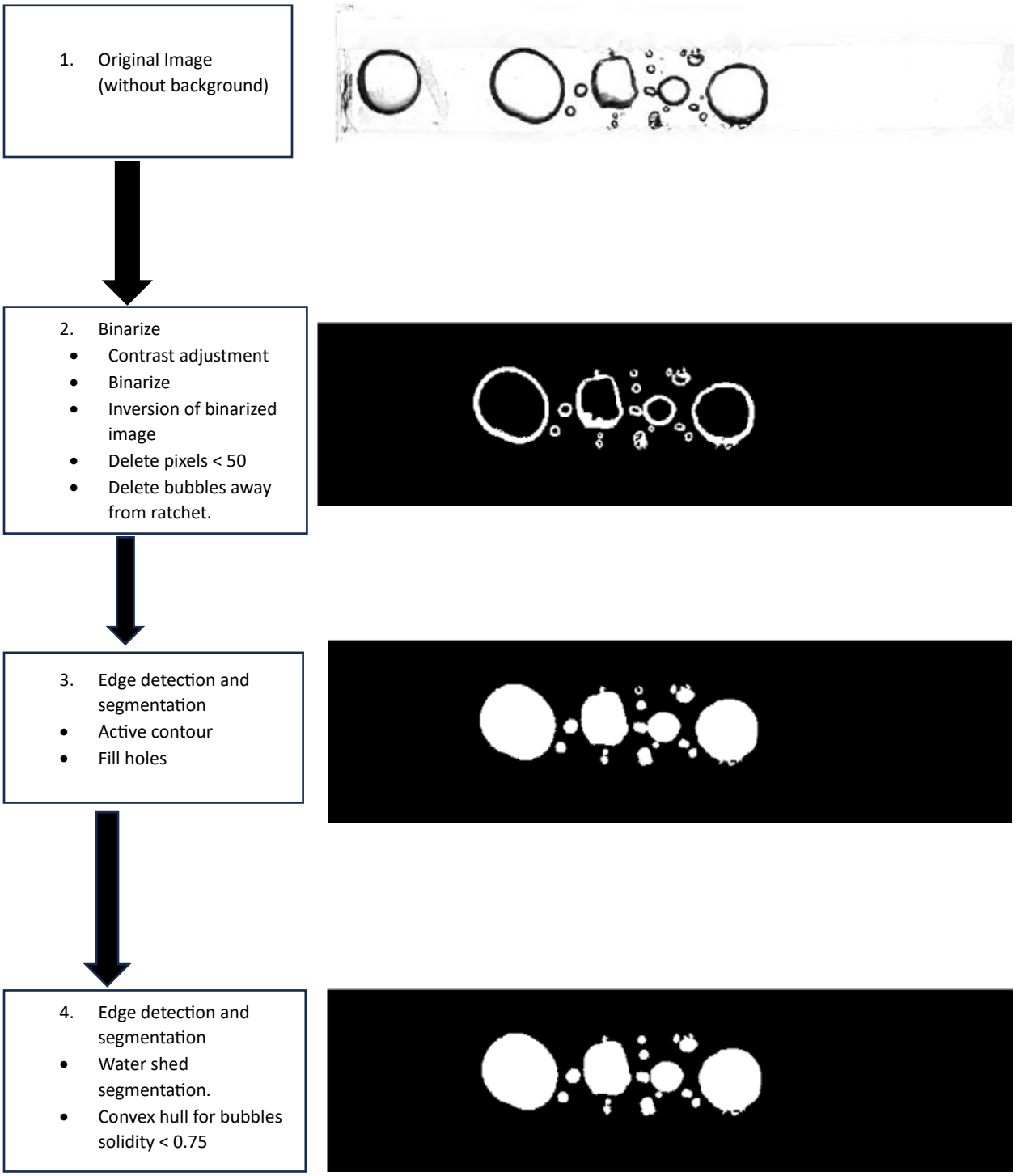

Figure 3-5: Series of images showing Image processing techniques for a single frame

Following segmentation and detection, the next step was to separate the bubbles that were attached to the ratchet at the nucleation site from the rest of the bubbles in the flow. For this, initially, the bubbles whose centroids were away from both top and bottom ratchets were deleted. For the remaining bubbles, to determine whether the bubble was attached to ratchet or not, a bounding box technique was used. The bounding box encapsulates each bubble in the smallest possible box, and the corner coordinates of these boxes can be obtained. This will give the position of the bubbles in the image. Figure 3-6 shows the illustration bounding box for one of the frames.

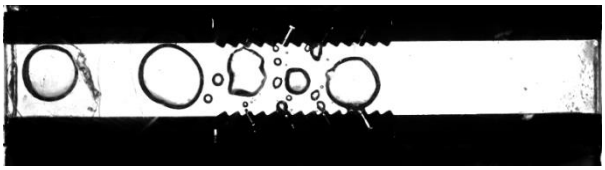

(a)

(b)

(c)

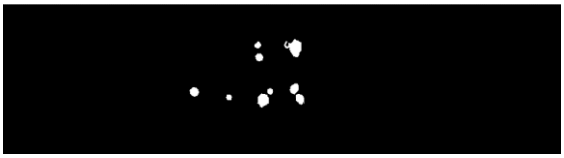

(d)

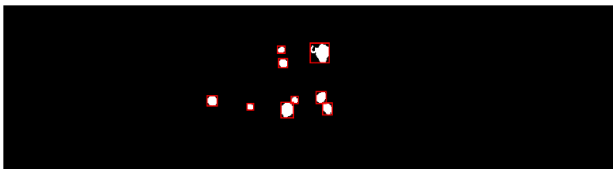

(e)

Figure 3-6: Image with Bounding box. (a) Original Tiff image, (b) Image with background deleted (c) Final Image after all Image processing techniques (d) Bubbles away from ratchet surface deleted (e) Bounding Box on the bubbles

Boundary coordinates of the bounding box were then compared with the coordinates of the ratchet face, which were obtained by graphing the ratchet manually using “ginput” in MATLAB. The ratchet faces where nucleation sites were located, were only considered so that the bubbles growing on the ratchet surface were detected, avoiding the bubbles attached to the surface where nucleation site was absent. For the top ratchet and the bubbles with y coordinate of centroid less than the half of the width of the channel , if the x coordinate of the top left corner of the bounding box was less than the ratchet’s x coordinate and the x coordinate of the top right corner of bounding box was greater than the ratchet’s x coordinate, with the y coordinate of the bottom corner greater than or equal to the y coordinate of the ratchet, the bubble was considered attached to the ratchet. The same logic was used for the bubbles near the bottom ratchet and is illustrated in figure 3-7. Each frame was divided into two frames: one with only bubbles attached to the ratchet as shown in figure 3-8 (1b, 2b, 3b,4b) and the other with bubbles that were not attached to the ratchet but were in the flow as shown in and figure 3-8 (1c,2c,3c,4c).

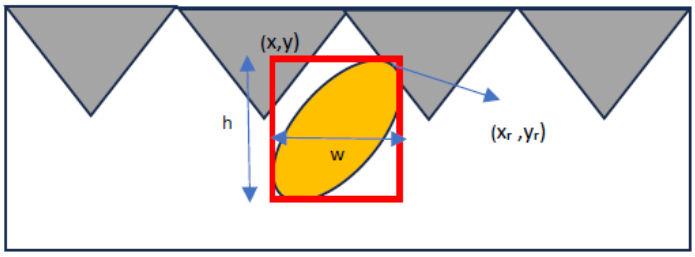

If $x_r > x$ and $x_r < (x+w)$ && $(y+h) => y_r$,

Then bubble is attached

Figure 3-7: Schematic of bubble with the bounding box (red box). (x_r,y_r) are coordinates of one of the points on ratchet and (x,y) is the coordinate of the bounding box with height h and width w

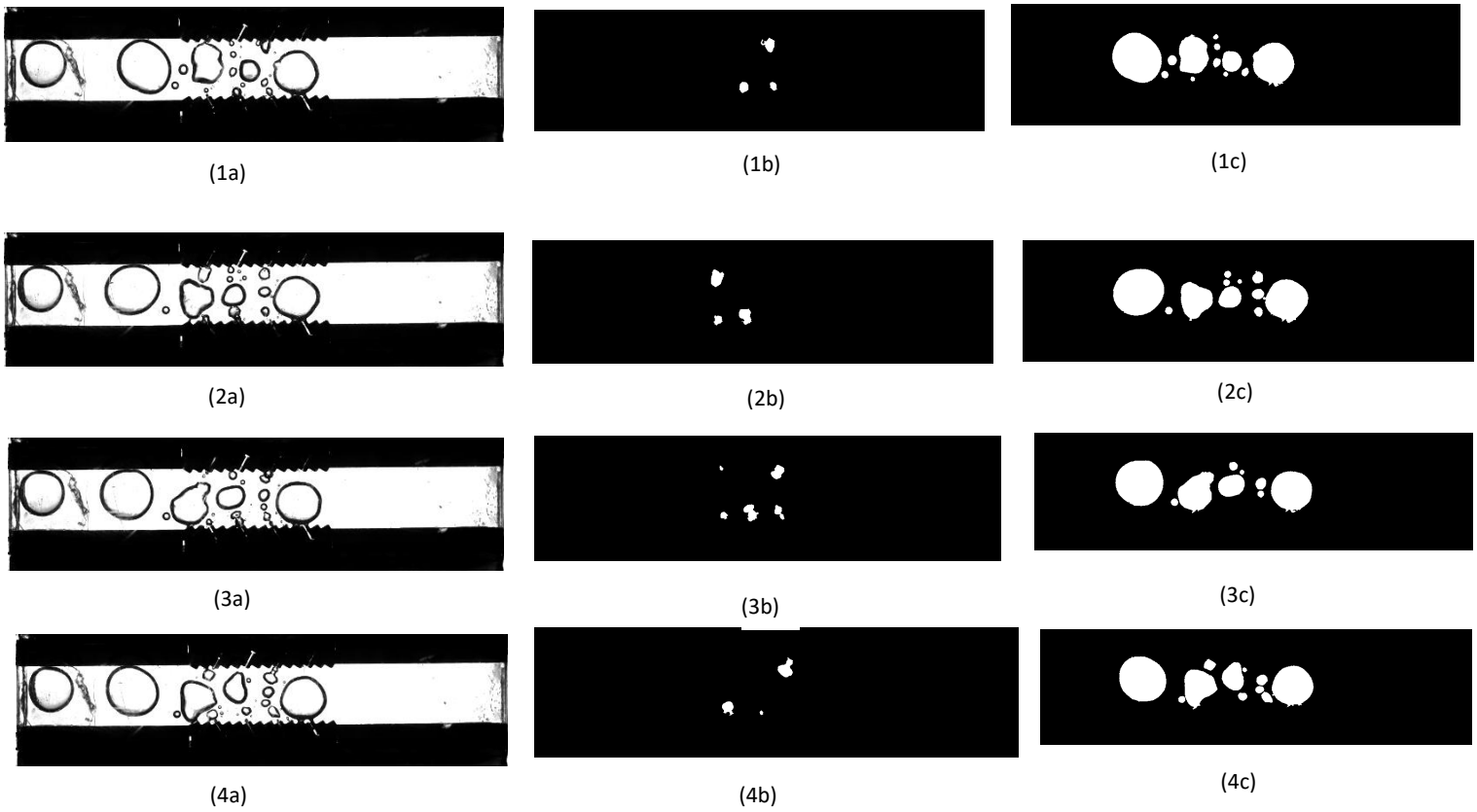

Figure 3-8: 1a, 2a, 3a, 4a: Original Tiff File & 1b, 2b, 3b, 4b: Frames with bubbles growing on ratchet & 1c, 2c, 3c, 4c: Frames with other bubbles in flow

3.2.2 Height & Diameter of the bubble

The frames, previously isolated with only bubbles attached to the ratchet, were considered for this step of the analysis. The height of the bubble at an angle equal to the nucleation site determines the velocity normal to the ratchet surface. The bubble height was defined as the distance between the nucleation site and the bubble boundary coordinate, which is at an angle equal to the angle of the nucleation site, as illustrated in Figure 3-9. Nucleation site coordinates were manually selected using 'ginput,' and the bubble boundary coordinates were obtained using 'bwboundary' in MATLAB.

Figure 3-9: Height of the bubble in reference to the nucleation site angle

The slope between the nucleation site and every coordinate on the bubble boundary was determined using the normal slope equation. About ten points on the bubble boundary, either making an angle equal to or closest to the angle of the nucleation site, were selected to account for any sway of the bubble away from the nucleation site. The distance of these ten points from the nucleation site was calculated, and the maximum distance among them was considered as the height of the bubble. Figure 3-10 illustrates this process for one of the points on the boundary of the bubble.

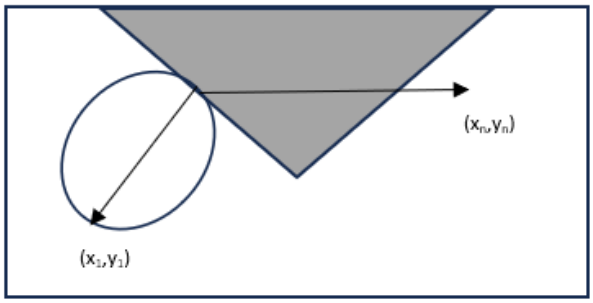

$$\text{Slope} = \frac{y_n - y_1}{x_n - y_n}$$

$$\text{Distance} = \sqrt{(x_n - x_1)^2 + (y_n - y_1)^2}$$

Figure 3-10: Schematic of calculation of slope and distance of a point on the boundary of bubble(x_1,y_1) with the nucleation site coordinate (x_n ,y_n). This calculation was conducted for every point on the boundary of the bubble.

If the height obtained was equal to or within the range of the major axis of the bubble, the minor axis was considered as the diameter. Conversely, if the height was equal to or within the range of the minor axis, the major axis was considered as the diameter. The lengths of the major and minor axes were obtained using 'regionprops' in MATLAB.

The height and diameter were stored as two separate arrays, each array with eight elements representing height or diameter of bubble at eight nucleation sites for each frame. The velocity imparted by the bubble was then calculated using this data and the empirical formula (eqn. 1.10). The velocity was calculated only for bubbles whose height and diameter were non-zero in consecutive frames. This eliminates departure velocities, providing only the velocity generated by the growing bubble. As the goal was to understand the lateral motion in the fluid, the horizontal component of the velocity was obtained using the angle of nucleation site.

3.3 Mean liquid velocity using PTV

The PTV algorithm, originally developed by Kapsenberg [14] to track bubbles departing from surfaces, was utilized for the mean velocity calculation. Frames without the bubbles growing on the ratchet were considered for the calculation of the mean flow velocity and the bubble tracking between two consecutive frames was conducted. The distance travelled by a bubble between two frames divided by the time elapsed (1/fps) results in the velocity of that bubble. The distance travelled was obtained from the difference in centroid locations of the bubble between consecutive frames. To ensure that the average velocity of all bubbles in a frame can be considered as the mean velocity of the flow, only bubbles within the regime of Stokes flow were tracked. The Stokes number (St) is given as:

$$St = \frac{\tau v}{d} = \frac{\rho_{v,sat} dv}{18\mu_{l,sat}}$$

(Eqn 3.9)

where τ is the relaxation time of particle, v is the velocity of flow, d is the diameter of the particle, $\rho_{v,sat}$ is density of the saturated vapor of fluid, $\mu_{l,sat}$ is the viscosity of the fluid. The density and viscosity values for FC 72 were shown in Appendix A.

For a Stokes number very less than 1 (St<<1), the particle will mostly follow the fluid. For St ~ 1 or St >> 1, the fluid has very less influence on the particle in the fluid [22]. For the velocities ranging from 10 mm/s

to 100 mm/s with a diameter of 1.25 mm, the Stokes number falls between $4.1x10^{-3}$ – $4.1x10^{-2}$. Since the St << 1, bubbles with a diameter of 1.25 mm were assumed to effectively follow the flow. Therefore, only bubbles with a diameter of 1.25 mm or less were considered for PTV.

The next step was to track these bubbles in consecutive frames. The centroid locations of the bubbles were determined in each frame. The nearest-neighbor approach was used to match the bubbles in frames A and B. For each bubble in frame A, the distance between its centroid and the centroid of every bubble in frame B was calculated. The bubble pair resulting in the minimum distance was considered a matched pair. To account for image processing errors, such as deletion or addition of bubbles and merging of bubbles, two constraints were added to verify the matched pairs. Each matched pair was checked for an area threshold (maximum area of matched pair bubbles/minimum area of matched pair bubbles) and a displacement threshold (distance between matched pair < displacement threshold), whose values will be discussed in the uncertainty analysis (Section 3.4). Matched pairs not meeting these constraints were deleted and not considered in velocity calculation.

With the distance traveled by each pair and the time elapsed between two frames now available, the velocity of each bubble was calculated. The horizontal component of this velocity was obtained using the slope between the centroid of matched pair bubbles. The average of the velocities of all the bubbles in a frame was equivalent to the mean velocity of the flow in that frame.

A summary flow chart of the algorithm used for the data analysis is shown below.

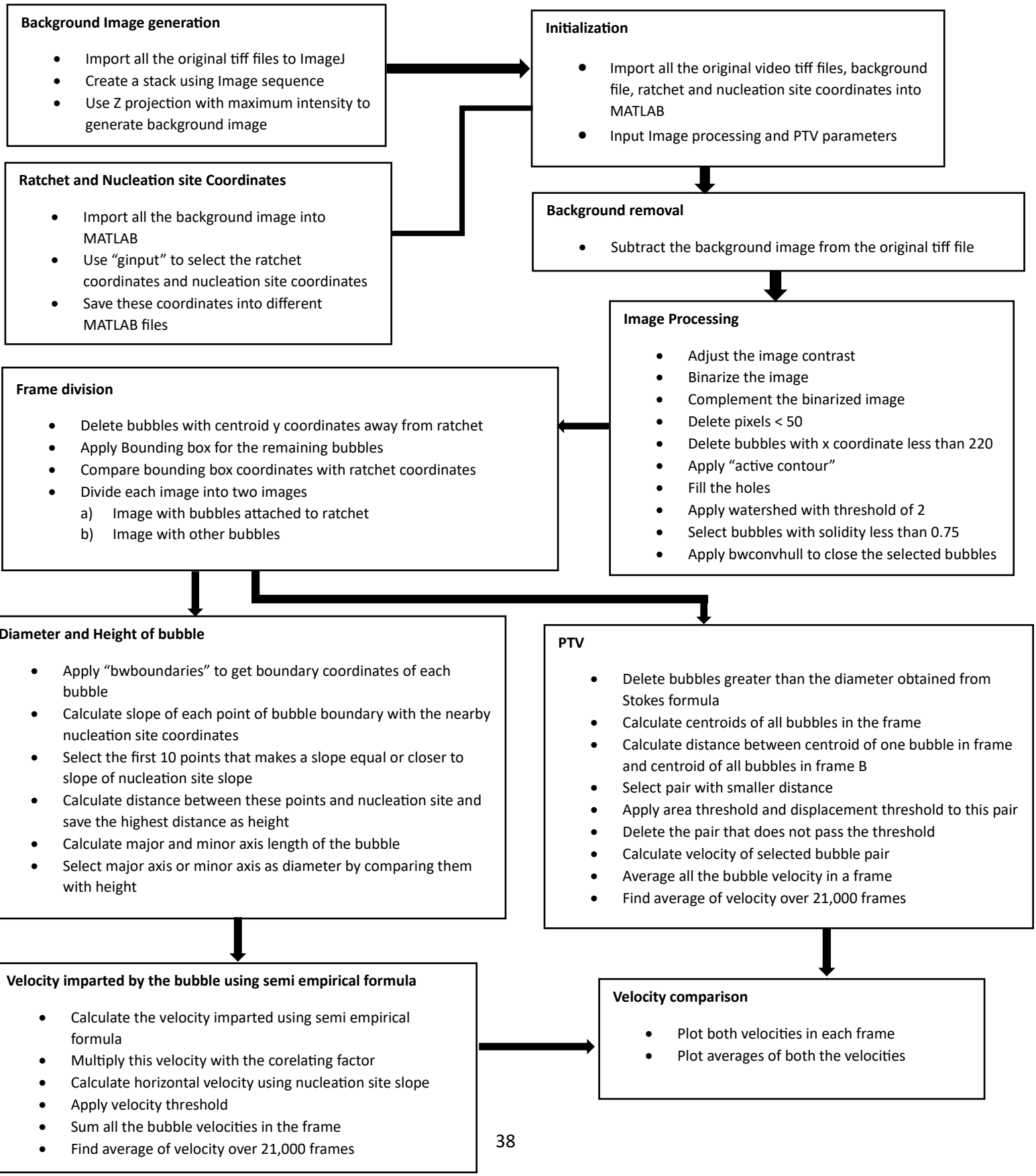

3.4 Uncertainty Analysis

To provide confidence in the data analysis, uncertainty analysis was carried out for the image processing and PTV algorithms. Errors may be generated by the inherent uncertainties in functions internal to MATLAB, such as determining centroid, diameter, major axis, and minor axis length, which cannot be quantified. However, since velocities were obtained over 21,000 frames, these errors can be neglected.

There were also uncertainties in the algorithm due to image processing input parameters like resolution, ratchet and nucleation site coordinates, and thresholding values. This section covers the effect of these parameters on both the velocity calculated from the empirical formula and the mean velocity of flow calculated from the PTV. The possible different parameters resulting in uncertainties are shown in the table 3-1.

Table 3-1: Uncertainties in Image Processing and PTV algorithms

S.No.	Parameter	Remarks
1.	Uncertainty in instruments used - Thermocouples - Pressure transducers - Ammeter - Voltmeter	This does not affect the velocity values
2.	Image Processing Inbuilt Uncertainties - Centroid, Major axis, Minor axis, Area, Solidity calculation - Bounding box generation - Edge detection errors - Segmentation errors	These errors were inbuilt in MATLAB and cannot be quantified. However, as both the velocities from semi empirical formula and PTV were averaged over 21,000 frames, these errors can be neglected
3.	Image Processing and PTV input values - Resolution - Ratchet and Nucleation site coordinates - Water Shed threshold - Solidity threshold - Displacement threshold - Area threshold - Velocity threshold	Effect of these parameters were verified by checking the difference in velocity resulted from varying the values of these parameters within reasonable bounds.

Resolution of the frame was calculated by comparing the distance between the two points in the frame in pixels to the distance between same two points measured on the reference geometry. The ratchets in the test section geometry were provided with a pitch of 1.5 mm. This measurement was used in comparison to the pixel values obtained from the frame. However, the pixel values were obtained manually by checking the distance between two different points in the image. To reduce the human error, the resolution values obtained from different point distances were averaged to get the final average resolution. Figure 3-11 shows the different distance values considered in the calculation of resolution.

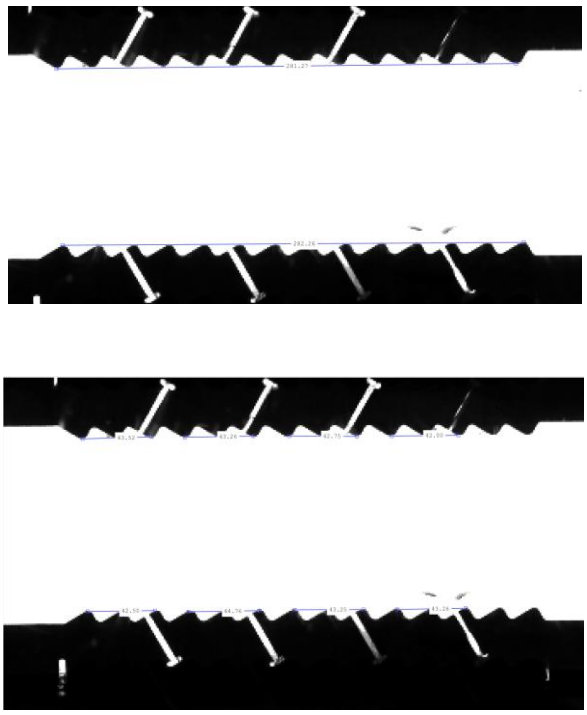

(a) Resolution with reference to channel length

Average length = 281.765 pixels

*Specimen length = 13*1.5 = 19.5 mm*

Resolution = 14 pixels/mm

(b) Resolution with reference to two crest distance

Average length = 43.1625 pixels

*Specimen length = 1.5*2 = 3 mm*

Resolution = 14 pixels/mm

Final Average Resolution = 14

Figure 3-11: Calculation of resolution of the frame

The ratchet coordinates and the nucleation site coordinates used in the algorithm to determine whether bubbles were attached to ratchet, were manually selected. To verify the effect of this uncertainty, the ratchet and nucleation site coordinates were randomly selected multiple times, and the velocities were calculated for these cases. The variation in velocities demonstrates the effect of uncertainty in this parameter. This analysis was carried over 100 frames. As can be seen from tables 3-2 and 3-3, the variation in the velocities was very small with respect to the ratchet and nucleation site coordinates.

Table 3-2: Variation in velocity due to ratchet coordinates for 100 frames

Case	Mean horizontal velocity imparted by growing bubble, mm/s	Variation in the velocity	Mean horizontal velocity from PTV, mm/s	Variation in PTV velocity
Trial 1	19.29	-0.71	32.73	0.22
Trail 2	19.63	-0.36	32.35	-0.16
Trial 3	19.95	-0.05	32.24	-0.27
Trial 4	20.75	0.76	32.79	0.27
Trial 5	20.36	0.36	32.46	-0.06
Average	20.00		32.52	

Table 3-3: Variation in velocity due to Nucleation site coordinates for 100 frames

Case	Mean horizontal velocity imparted by growing bubble, mm/s	Variation in the velocity	Mean horizontal velocity from PTV, mm/s	Variation in PTV velocity
Trial 1	14.88	-0.07	31.88	0
Trial 2	14.88	-0.06	31.88	0
Trial 3	15.20	0.26	31.88	0
Trial 4	14.85	-0.10	31.88	0
Trial 5	14.92	-0.03	31.88	0
Average	14.95		31.88	

In image processing, for the watershed segmentation, a threshold value was specified for the sensitivity of determining nearby bubbles. The variation in velocity values stabilized and remained constant for threshold values equal to or greater than 2 as shown in table 3-4 and thus the same was selected for analysis of all image series.

Table 3-4: Variation in velocity due to water shed threshold for 100 frames

S.No.	Water shed threshold value	Mean horizontal velocity imparted by growing bubble, mm/s	Mean velocity from PTV, mm/s
1.	1.25	17.30	31.81
2.	1.5	17.30	31.81
3.	1.75	14.83	31.88
4.	2	14.83	31.88
5.	2.25	14.83	31.88
6.	2.5	14.83	31.88

Solidity threshold of 0.75 was used in the image processing to segregate the bubbles that were not closed properly and apply the convex hull. It was observed that a solidity threshold of 1 would alter the shapes of the bubbles applying the convex hull for most of the objects in a frame and a solidity threshold less than 0.7 would not detect all the bubbles that were unclosed. Hence a value of 0.75 is selected. The variation of velocities with the solidity threshold are shown in the table 3-5.

Table 3-5: Variation in velocity due to Solidity threshold for 100 frames

S.No.	Solidity threshold value	Mean horizontal velocity imparted by growing bubble, mm/s	Mean velocity from PTV, mm/s
1.	0.5	15.19	31.77
2.	0.6	15.19	31.77
3.	0.75	14.83	31.88
4.	0.8	14.61	31.89
5.	1	16.37	37.40

Displacement and area thresholds, as previously discussed, play a pivotal role in facilitating accurate matching of bubbles within the Particle Tracking Velocimetry (PTV) algorithm across consecutive frames. Notably, the displacement threshold value, set at one pixel to constrain bubble displacement between successive frames, demonstrates negligible influence on velocities as shown in table 3-6. Meanwhile, the area threshold, as evidenced in the table 3-7, exhibited an impact on velocities. To enhance the efficiency of bubble pair identification across frames, a conservative allowance of 5% change in bubble area was imposed. Consequently, a value of 1.05 was adopted for the area threshold.

Table 3-6: Variation in velocity due to Displacement threshold for 100 frames

S.No.	Displacement threshold value	Mean horizontal velocity imparted by growing bubble, mm/s	Mean velocity from PTV, mm/s
1.	0.8	22.21	27.18
2.	0.95	22.21	27.18
3.	1	22.21	27.18
4.	1.05	22.21	27.18
5.	1.1	22.21	27.18
6.	0.8	22.21	27.18

Table 3-7: Variation in velocity due to Area threshold for 100 frames

S.No.	Area threshold value	Mean horizontal velocity imparted by growing bubble, mm/s	Mean velocity from PTV, mm/s
1.	1	22.22	0.00
2.	1.05	22.22	27.18
3.	1.1	22.22	27.92
4.	1.15	22.22	28.07
5.	1.2	22.22	28.10
6.	1.25	22.22	28.11

The image processing was conducted on all the 21,000 frames for each condition. As it was not possible to provide different image processing parameters depending on each frame, same parameters were used throughout 21,000 frames. This uniform parameterization resulted in varying effectiveness across frames leading to improper bubble detection in some of the frames as shown figure 3-12. This ineffectiveness generated the inadequacies in the height and diameter values which in turn lead to higher velocity values from the semiempirical equation (eqn. 1.10). To mitigate these errors and increase reliability on the results, a threshold value was applied to the horizontal velocity resulted from the semi empirical formula. Any velocity higher than this threshold value, is suppressed to reduce errors.

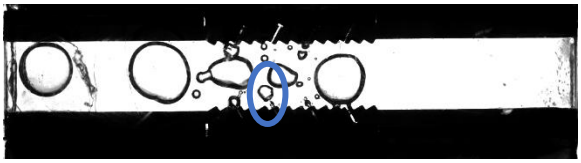

Frame 100 – Original Tiff file

Frame 100 – Image with bubbles attached to ratchet

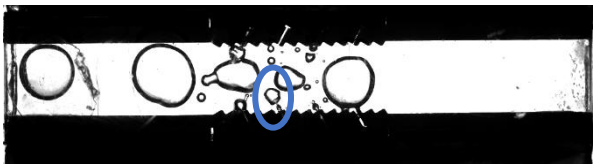

Frame 101 – Original Tiff file

Frame 101 – Image with bubbles attached to ratchet

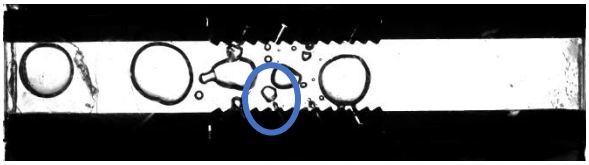

Frame 102 – Original Tiff file

Frame 102 – Image with bubbles attached to ratchet

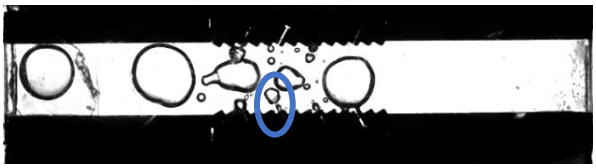

Frame 103 – Original Tiff file

Frame 103 – Image with bubbles attached to ratchet

Figure 3-12: Errors in Image Processing

As seen in figure 3-12, the second bubble from the bottom left had errors in segmenting. In frame 100, the algorithm detected the bubbles as different and has shown one of them as attached to the ratchet. Whereas in frame 101 and 102, they were detected as merged and immediately in frame 103, they were detected as separate. This resulted in a larger change in height and diameter values resulting in a horizontal component of velocity of 500 mm/s. To reduce these errors velocity threshold filter was applied. A threshold between 100 – 300 mm/s has maintained lower errors with less effect on the mean of the velocity as shown in table 3-8. Thus, a velocity threshold of 200 mm/s was considered. Any horizontal velocity imparted by growing bubble obtained from semi empirical formula greater than 200 mm/s was suppressed to zero reducing the image processing errors.

Table 3-8: Variation in velocity due to Velocity threshold for 1000 frames

S.No.	Velocity threshold value	Mean horizontal velocity imparted by growing bubble, mm/s	Mean velocity from PTV, mm/s
1.	No condition	48.63	27.18
2.	500	43.67	27.18
3.	400	37.30	27.18
4.	300	27.80	27.18
5.	200	23.08	27.18
6.	100	22.21	27.18
7.	80	21.59	27.18
8.	50	20.18	27.18

CHAPTER 4 RESULTS AND DISCUSSION

This section presents the results of the data analysis conducted on high-speed images obtained from the experiments, utilizing image processing and particle tracking velocimetry techniques discussed in the previous chapter. Initially, a qualitative description of the bubble motion for all cases is provided, followed by a comparison of the average velocities obtained from semi empirical formula (eqn 1.10) and PTV for each case using the equation described in Data Analysis section (eqn. 3.8). This comparison provides a validation for both the bubble pumping concept and the semi empirical formula. Additionally, Safarkoolan and Odele (unpublished work) calculated the velocity of the slugs (bubbles whose length is more than the channel width) using PTV technique, and this velocity will also be compared with the results obtained from the data analysis.

4.1 Qualitative Visualization

The experiment was conducted on six different cases of heat flux and subcooling. One case was with the reversed direction of nucleation sites, which was conducted to validate that the bubble growth on ratchet surface facilitates fluid motion in a preferential direction. A qualitative visualization of bubble dynamics in the original Tiff files obtained from the experiments is provided for each case.

4.1.1 High Subcooling High Heat flux (HSHH)

For high subcooling and high heat flux condition, the experiment was conducted at a high heat flux of 2.47 W/cm^2 and at subcooling of 10.52 ^0C. The images in figure 4-1 show the bubble dynamics in this condition.

t = 0 s

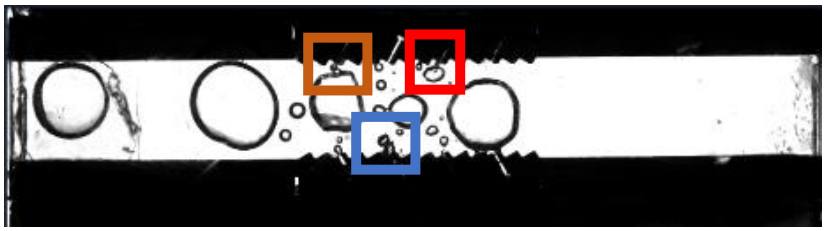

t = 7 ms

t = 11 ms

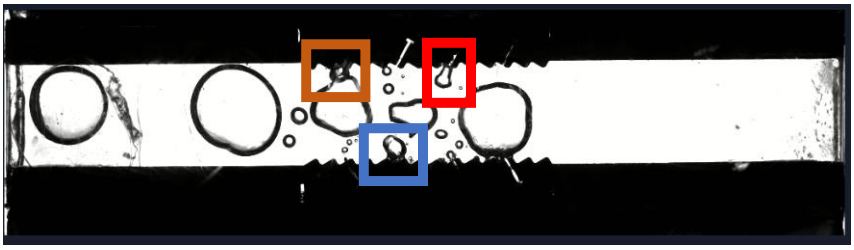

t = 14 ms

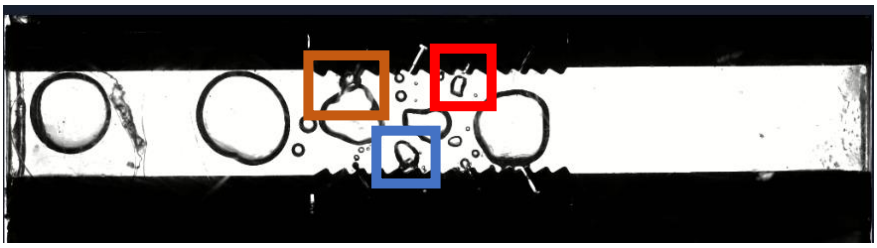

t = 16 ms

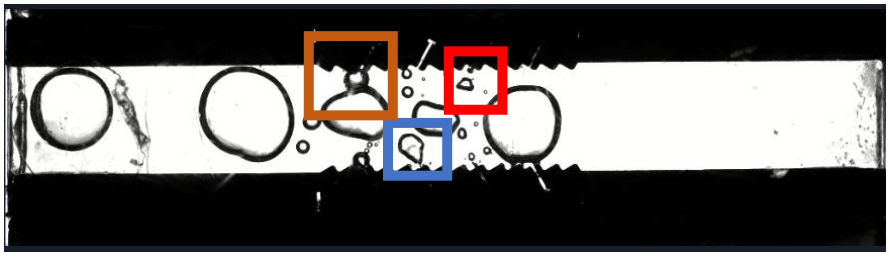

t = 22 ms

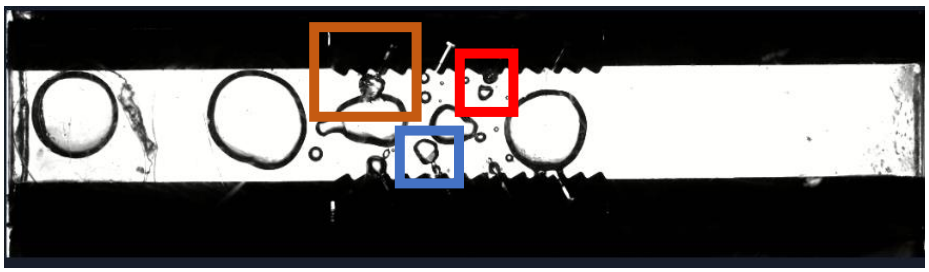

t = 26 ms

Figure 4-1:Sequence of frames at high subcooling high heat flux

Figure 4-1 illustrates the generation of bubbles for time frames, t =0,7,11,14,16,22,26 ms at nucleation sites, specifically the first and third nucleation sites from the left on the top ratchet, and the second nucleation site from the left on the bottom ratchet. These sites were highlighted in the figure. Bubbles develop and grow normal to the 30° slope and continue to move left side with an angle equal to angle of nucleation site after detaching from the ratchet. As the bubble grows on the ratchet, it consistently merges with multiple bubbles originating from the same cavity reaching the departure diameter or merges with the other bubbles in the flow. Following several coalescence events, buoyancy forces eventually carry the larger bubble away from the ratchet. Coalesced large bubbles move in the direction of the shallow slope of the ratchet (from right to left).

4.1.2 High Subcooling Mid Heat flux (HSMH)

The high subcooling and mid heat flux condition was conducted at a heat flux of 1.40 W/cm^2 and at a subcooling of 10.8 ^{0}C.

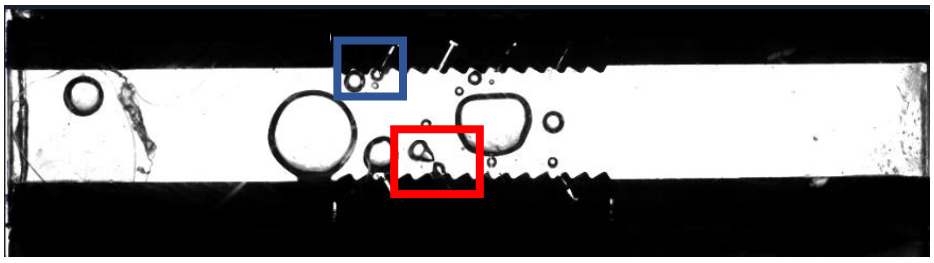

t = 0 s

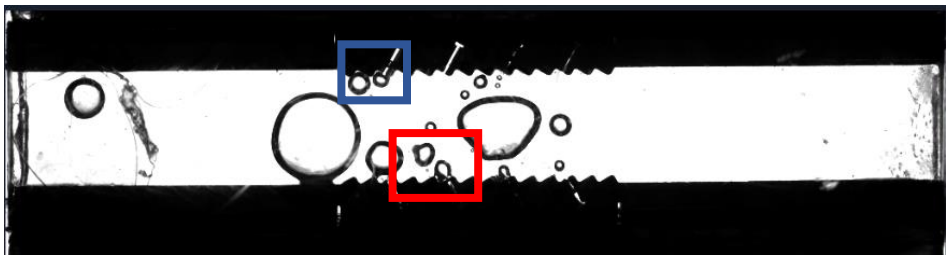

t = 8 ms

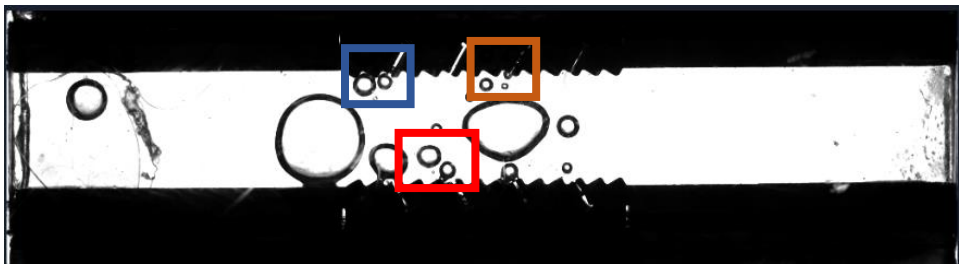

t = 16 ms

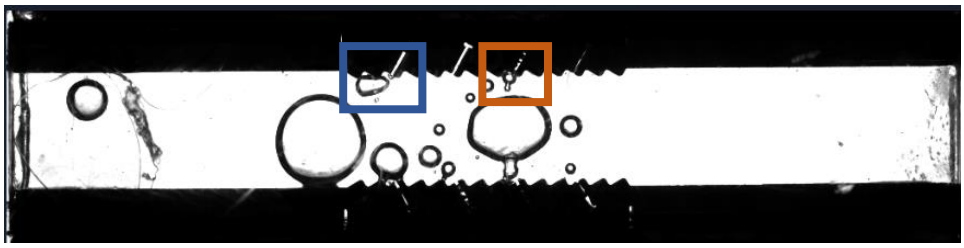

t = 25 ms

t = 35 ms

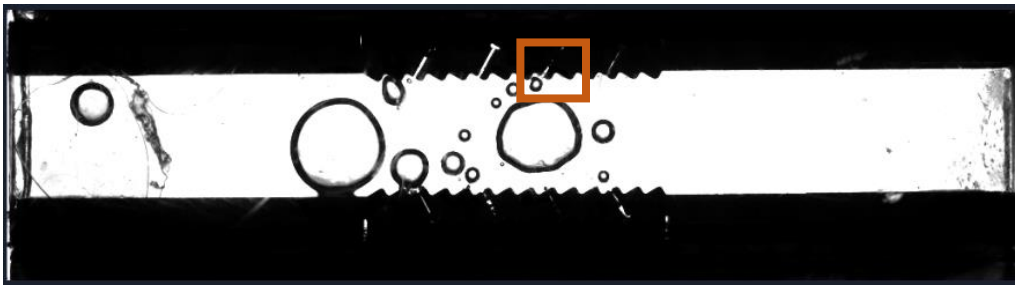

t = 40 ms

Figure 4-2: Sequence of frames at high subcooling mid heat flux

Based on the images in figure 4-2, the bubbles nucleate and grow predominantly at the first and third nucleation sites from the left on the top ratchet, and the second nucleation site from the left on the bottom ratchet. As observed in the previous condition, the bubbles in this condition too moved towards left side at an angle equal to angle of nucleation site after departure from the nucleation site. In comparison with the high subcooling and high heat flux condition, the departure diameters and the coalescences required for the bubble departure are smaller in this condition.

4.1.3 Mid Subcooling Mid Heat flux (MSMH)

Under conditions of mid subcooling and mid heat flux, observed at a heat flux of 1.48 W/cm^2 and a subcooling of 5.7°C, bubbles ebullition was observed from the ratchet cavities. These bubbles coalesced with larger bubbles in the flow, creating a slug. A bubble with a diameter exceeding 9 mm (equal to width of channel) was identified as a slug. The formation of these slugs is visually captured in the sequence of images presented in figure 4-3. Slugs predominantly moved towards the left side. However, the complex merging of bubbles into various shapes posed a challenge for segmentation and tracking using the algorithm. To efficiently analyze these images, there is a need for higher sensitivity models capable of accurately segmenting closely positioned bubbles.

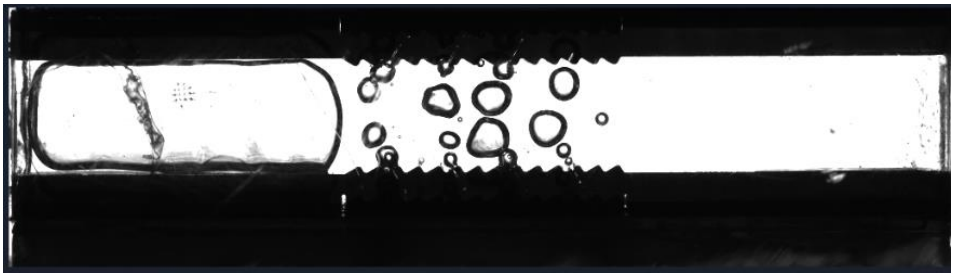

t = 0 s

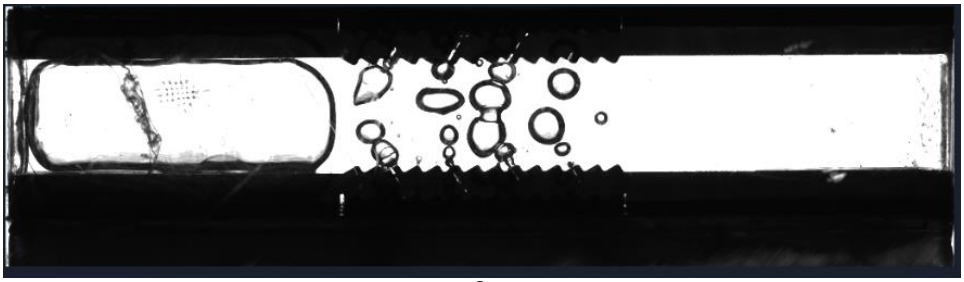

t = 9 ms

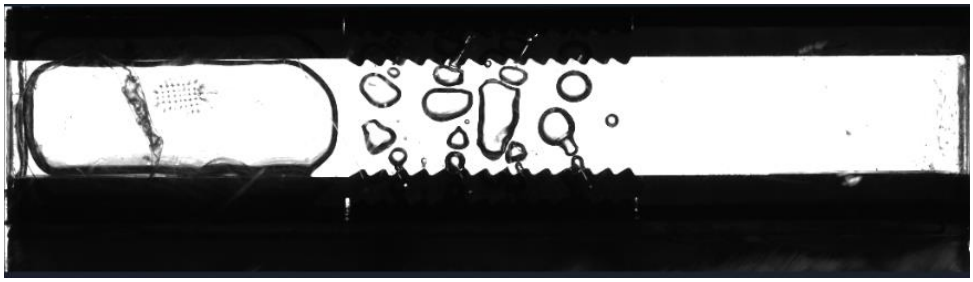

t = 17 ms

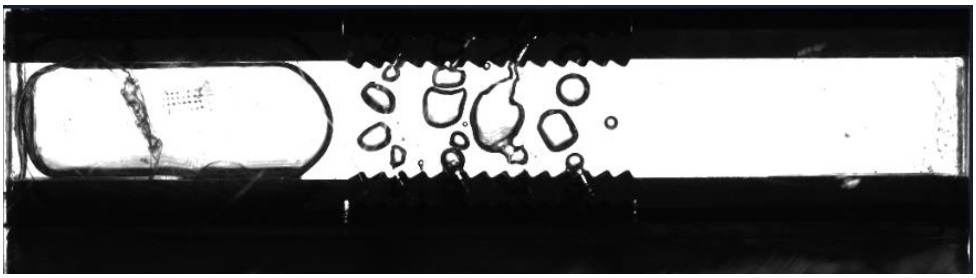

t = 26 ms

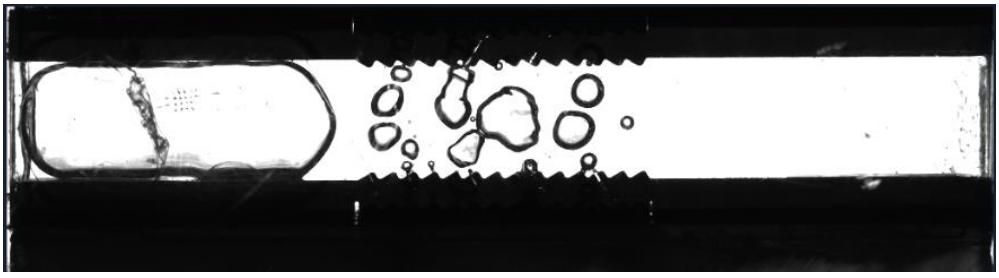

t = 36 ms

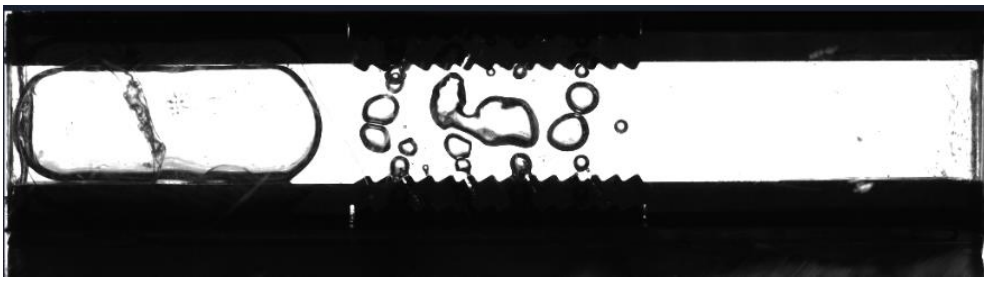

t = 46 ms

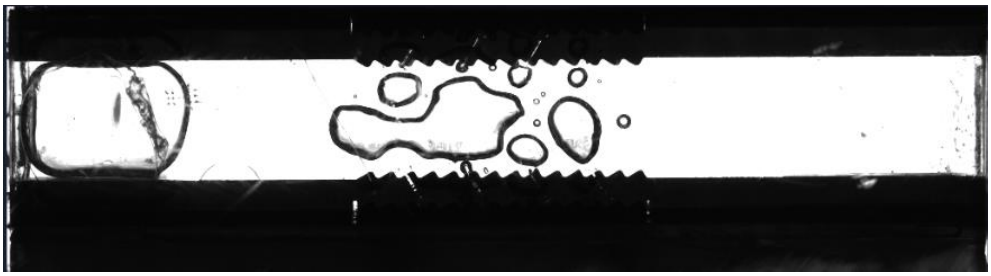

t = 260 ms

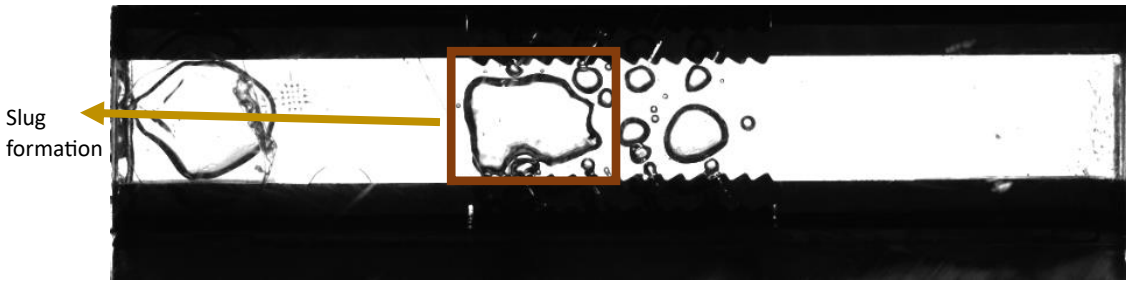

t = 330 ms

Figure 4-3: Sequence of frames at mid subcooling mid heat flux

4.1.4 Low Subcooling Mid Heat flux (LSMH)

The condition of low subcooling and mid heat flux, was obtained at a heat flux of 1.33 W/cm^2 and a subcooling of 2.76°C. In this condition, slugs were observed to form because of the merging of bubbles, similar to the phenomenon observed in the mid subcooling mid heat flux condition. However, a distinctive feature was noted: the bubbles growing on the ratchet were exceptionally large in this condition. The bubbles emerging from the nucleation sites on the top and bottom merged to form a much larger slug. This enlarged slug extended the entire length of the ratchet, with the bubbles from the nucleation sites merging with the slug from top and bottom and moving it towards the left side. The rapid and intricate

nature of bubble merging presented challenges for the current algorithm, making it difficult to differentiate between the slug and the bubbles originating from the nucleation sites. Consequently, this condition was excluded from the analysis. For a large portion of the experiment, the slugs covered the entire ratchet area. Fortunately, there were few frames as shown in figure 4-4, where the bubble merging into slug could be observed.

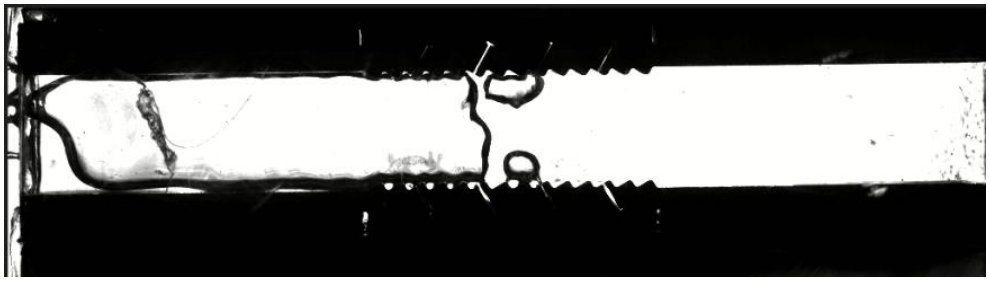

t = 500 ms

t = 521 ms

t = 533 ms

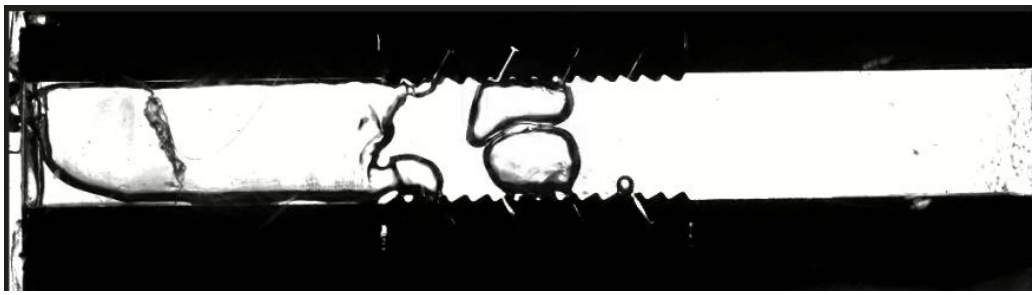

t = 553 ms

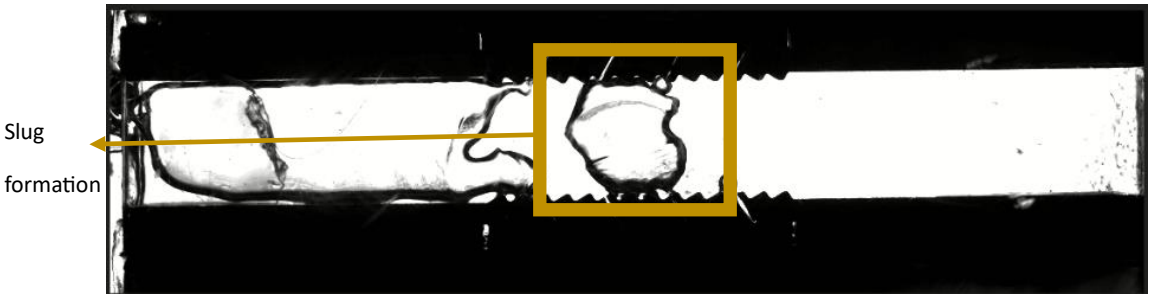

t = 560 ms

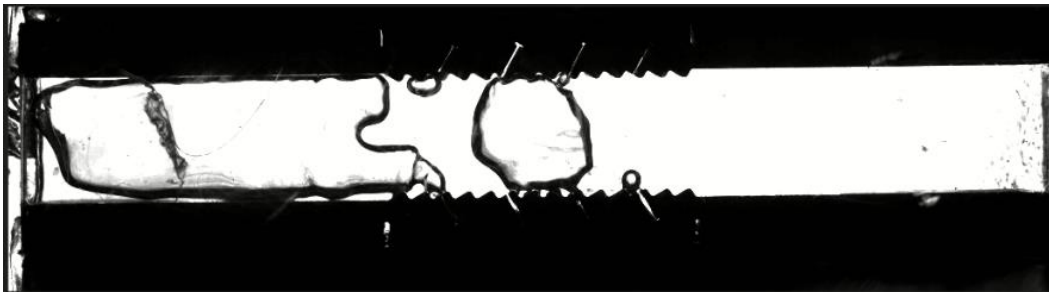

t = 571 ms

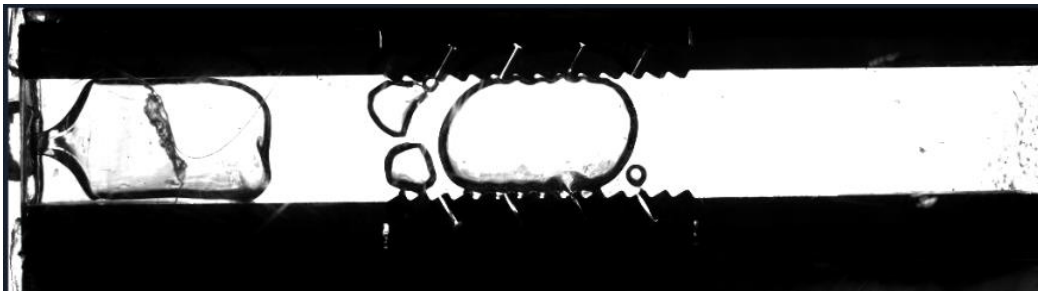

t = 680 ms

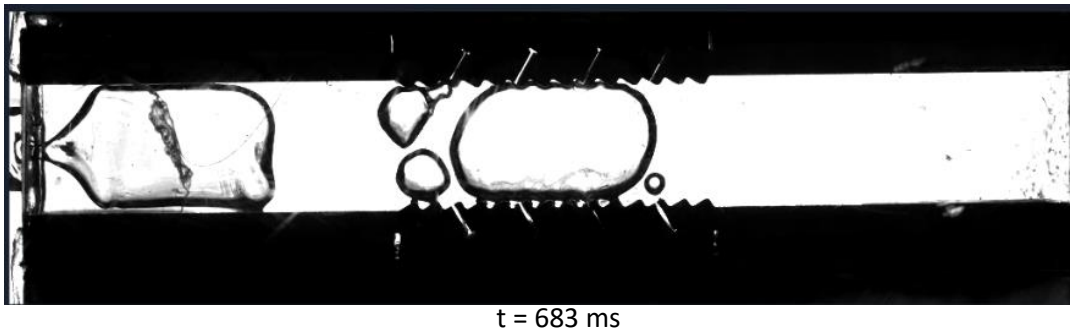

t = 683 ms

Bubble generating from the nucleation site merging with the slug

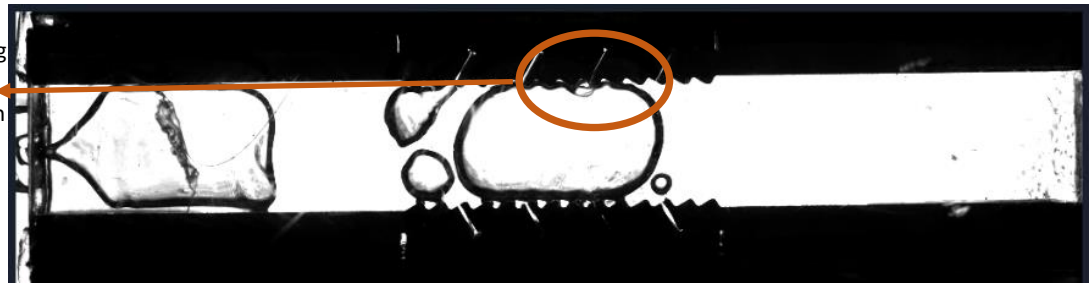

t = 686 ms

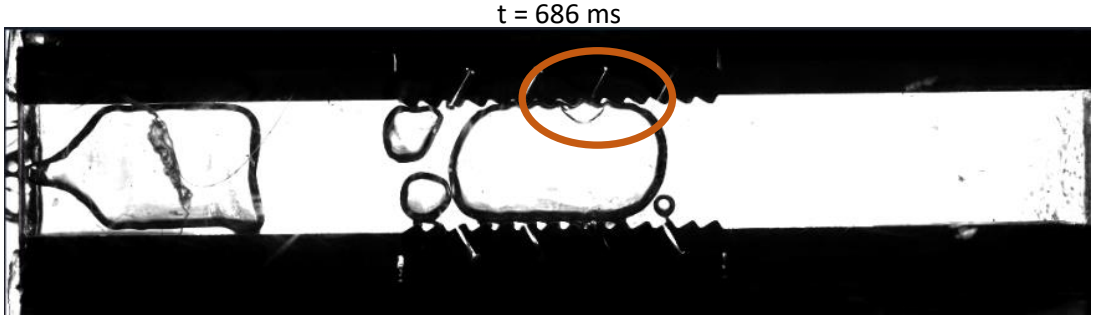

t = 690 ms

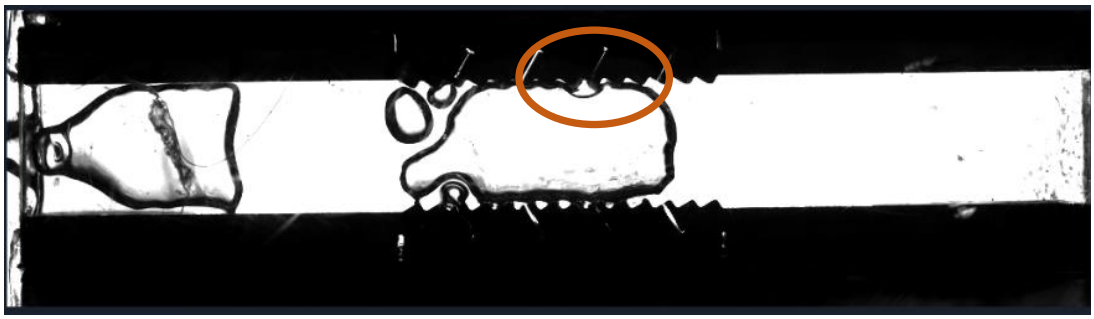

t = 706 ms

Figure 4-4: Sequence of frames at mid subcooling mid heat flux

4.1.5 Low Subcooling Low Heat flux (LSLH)

The condition of low subcooling and low heat flux was established at a heat flux of 0.86 W/cm^2 and a subcooling of 2.3 °C. In this condition, slugs were generated through the merging of bubbles, similar to the observed phenomena in the mid subcooling mid heat flux and low subcooling mid heat flux conditions. However, the slug formation in this instance was not as immediate as in the low subcooling and mid heat flux condition. Larger bubbles were observed to nucleate on the ratchet in comparison to the mid subcooling and mid heat flux condition. As anticipated, the formed slugs exhibited a leftward movement. A sequence of images illustrating this condition is presented in figure 4-5.

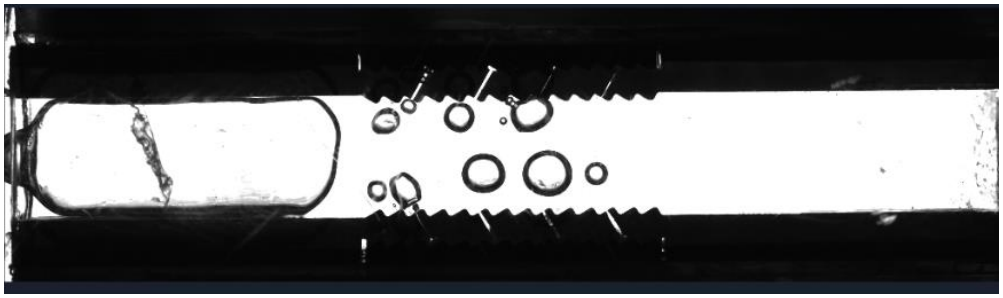

t = 30 ms

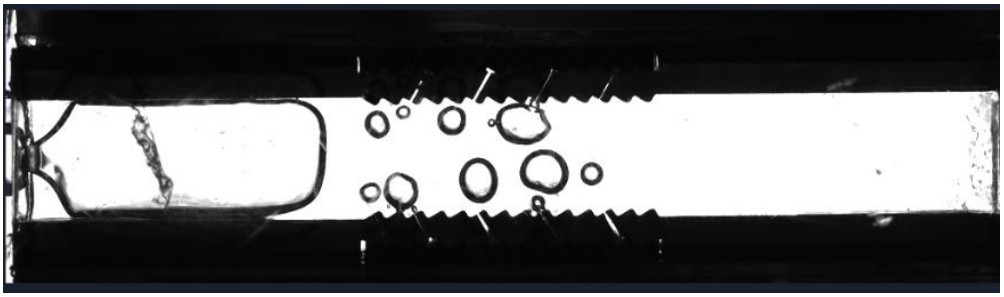

t = 46 ms

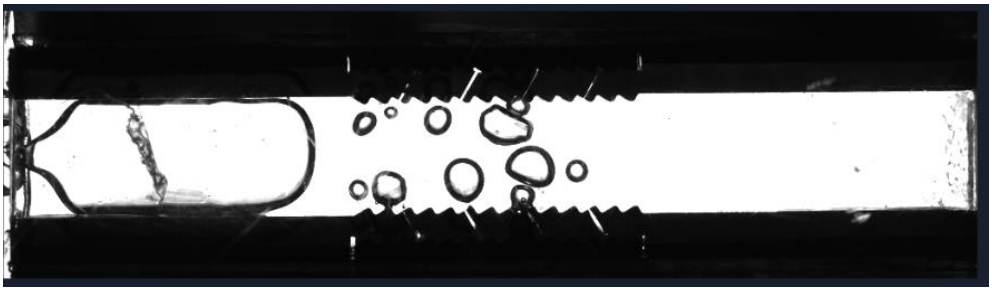

t = 52 ms

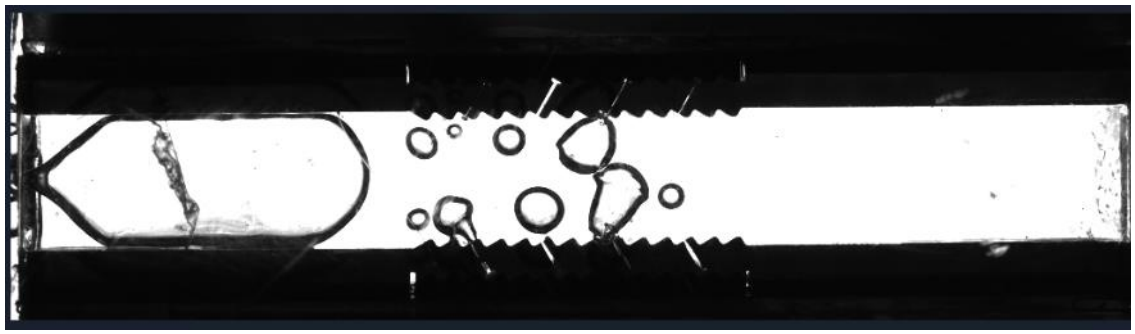

t = 62 ms

t = 143 ms

t = 185 ms

t = 192 ms

t = 207 ms

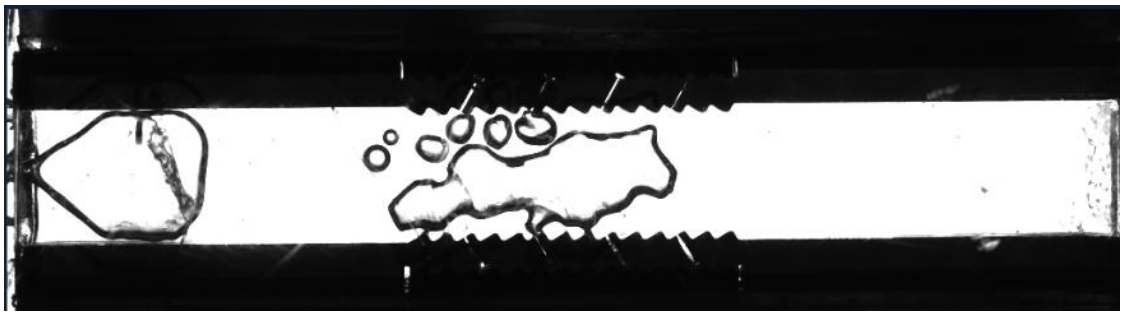

t = 225 ms

Figure 4-5: Sequence of frames at low subcooling low heat flux

4.1.6 High Subcooling High Heat Flux – Reverse (HSHH – R)

The high subcooling and high heat flux condition, coupled with a 180-degree change in the orientation of the ratchets, was executed to validate that the growth of bubbles on the ratchet induces fluid motion in a preferential direction. This condition involved a heat flux of 2.62 W/cm^2 and a subcooling of 9.65 °C. The bubbles grow on the ratchet normal to the 30-degree slope and, upon detachment, followed an angle equal to the nucleation site angle, leading towards the right side. To illustrate the preferential direction movement, the trajectory of a one of the bubbles was tracked, as depicted in figure 4-6.

t = 0 ms

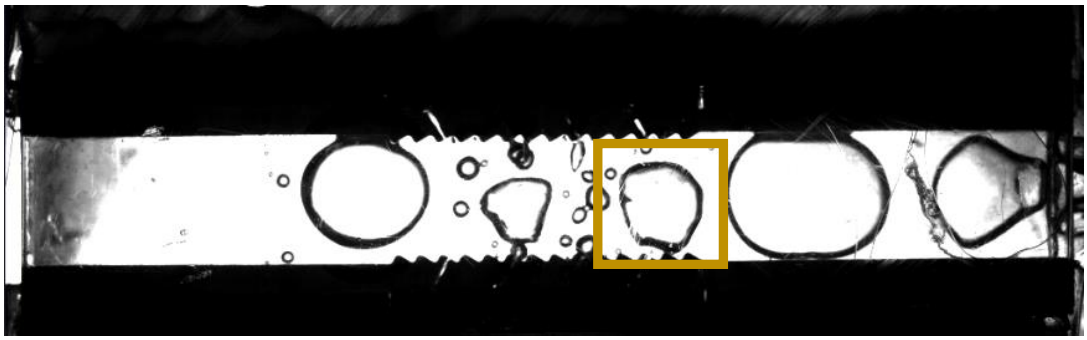

t = 110 ms

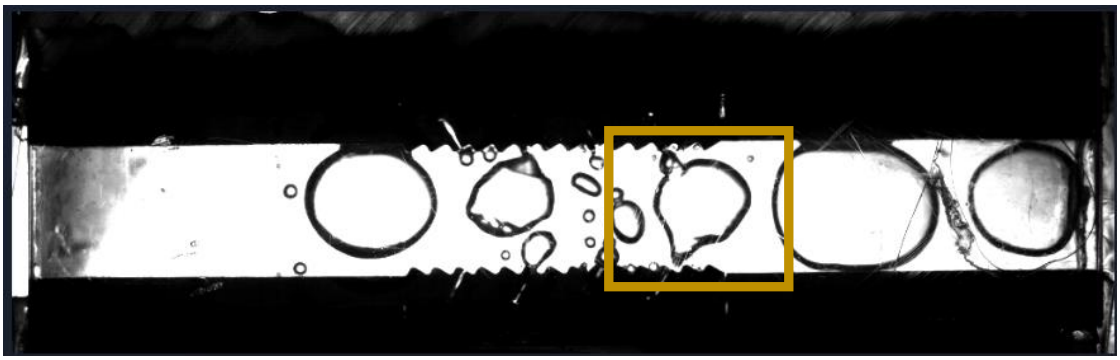

t = 250 ms

t = 375 ms

t = 500 ms

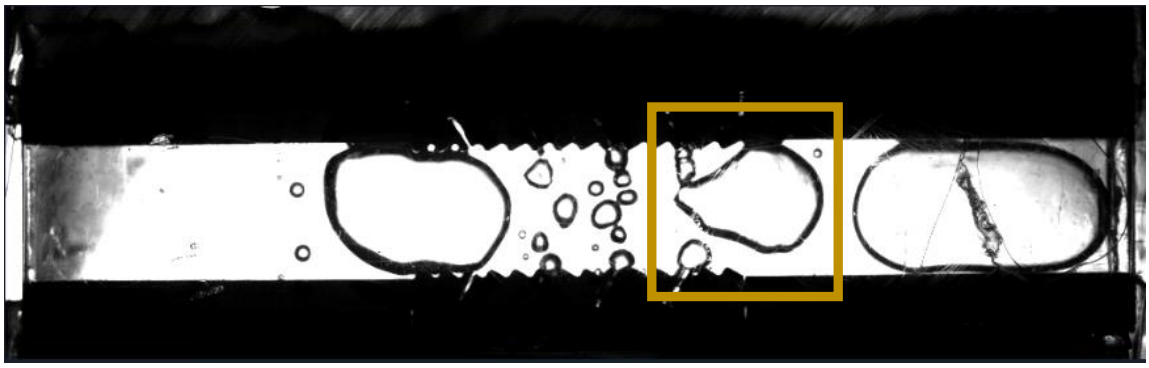

t = 620 ms

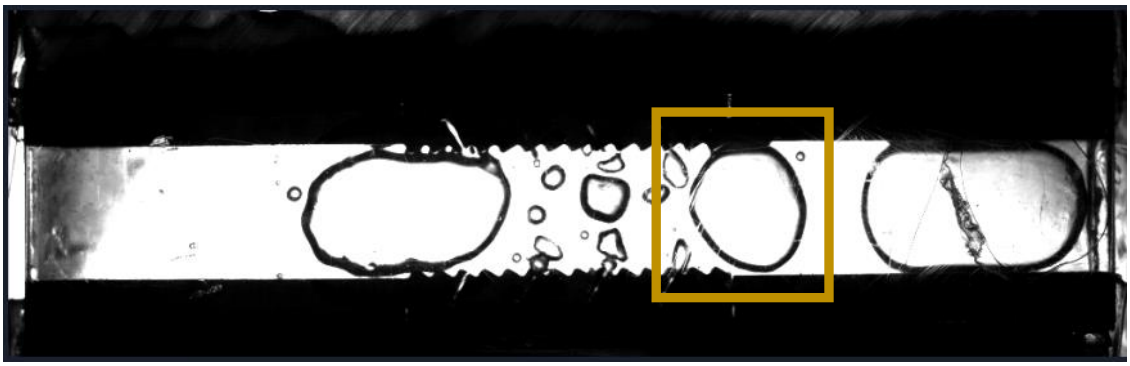

t = 750 ms

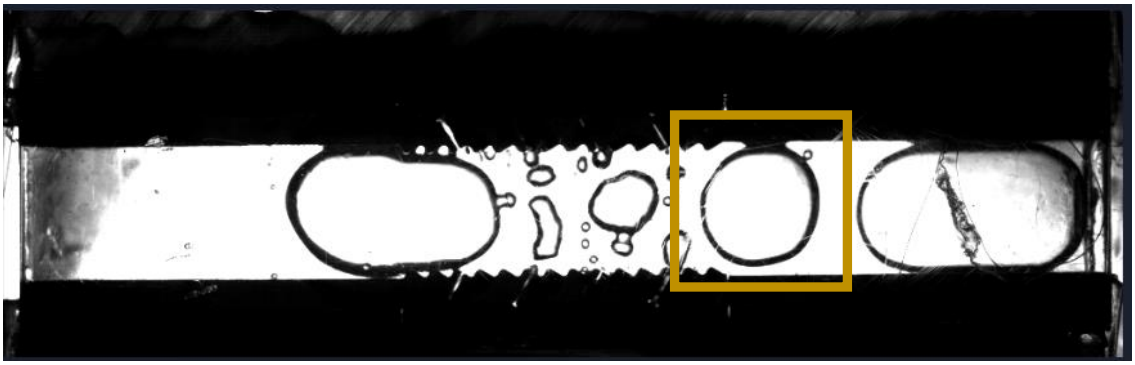

t = 875 ms

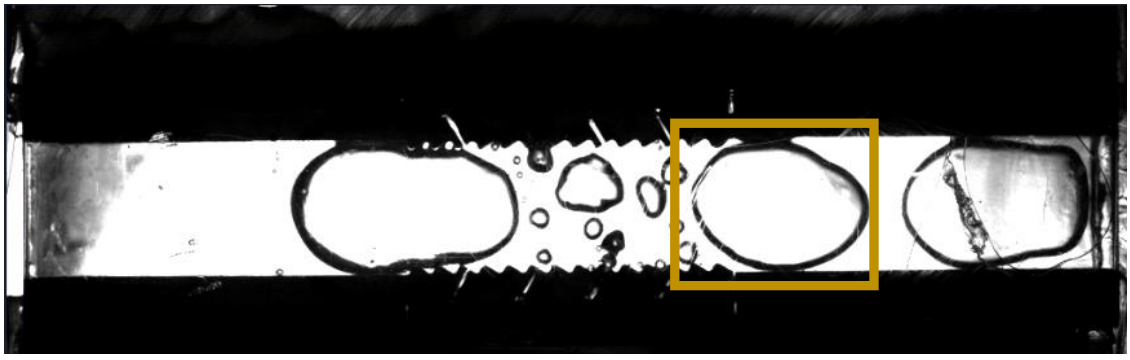

t = 1250 ms

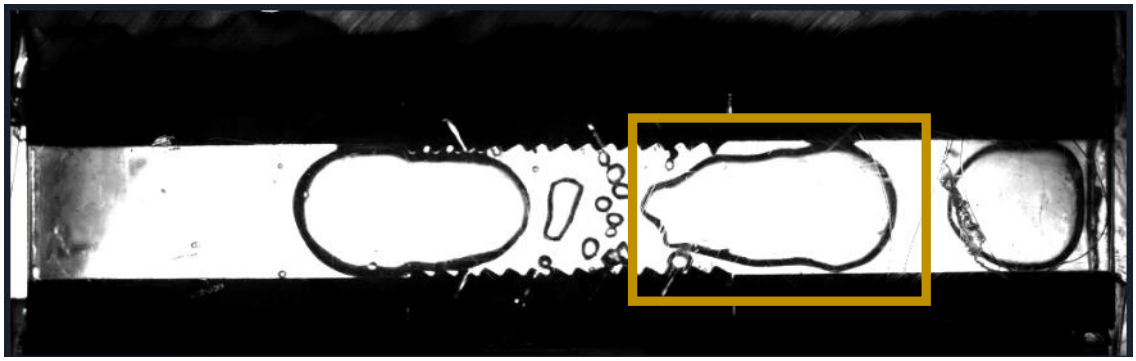

t = 1500 ms

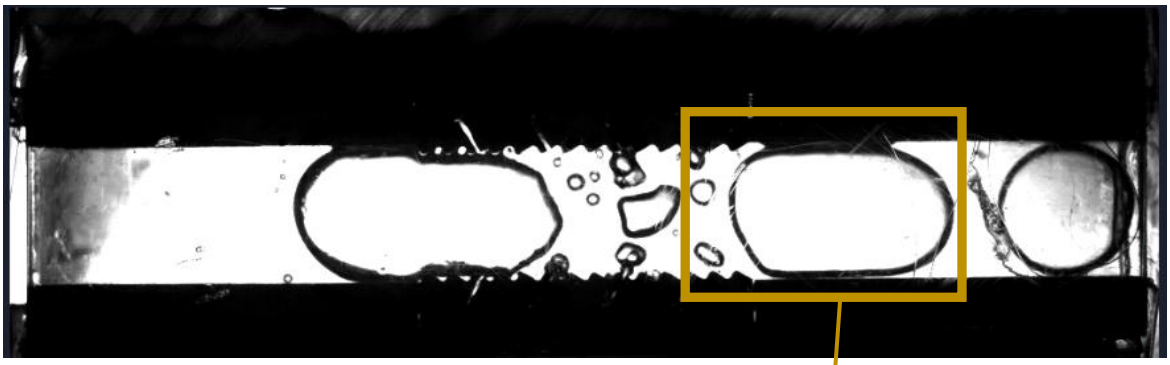

t = 1750 ms

Initial bubble merged with other bubbles in the flow forming a slug and moved towards right side

Figure 4-6: Sequence of frames for High subcooling and high heat flux with ratchet reverse condition

As seen from figure 4-6, the bubbles started to grow on the ratchet, merged with other bubbles in the flow forming a slug and moved towards right side. This observation confirms that the growth of bubbles on the ratchet indeed promotes the preferential movement of liquid in a specific direction.

All the above conditions with the bubble dynamics defining them are summarized in figure 4-7 below.

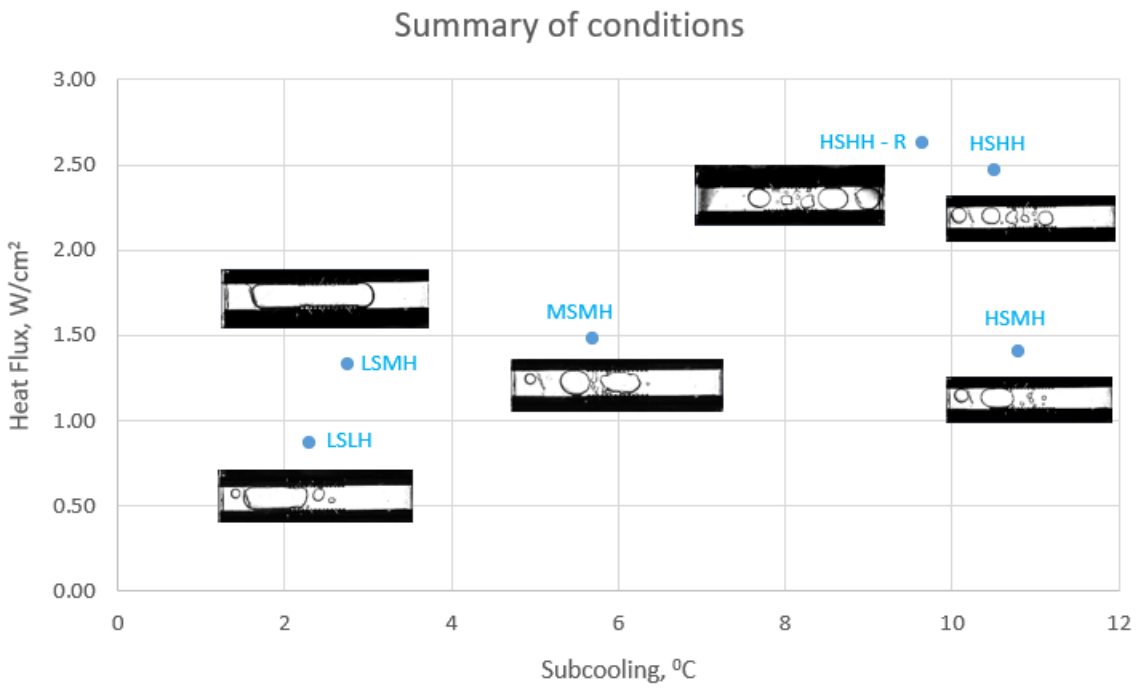

Figure 4-7: Summary of Conditions

4.2 Horizontal Velocity comparison

The algorithm described in Chapter 3 was used to obtain horizontal velocity imparted by the bubble growing on the ratchet using the semi empirical formula (eqn. 1.10). This velocity was adjusted for the entire ratchet area using the equation (eqn. 3.8). Smaller bubbles in the flow were tracked to calculate the mean velocity of flow in each frame using the PTV technique. The adjusted horizontal velocity from the semi empirical formula and the horizontal velocity from PTV were compared to validate the concept of bubble pumping.

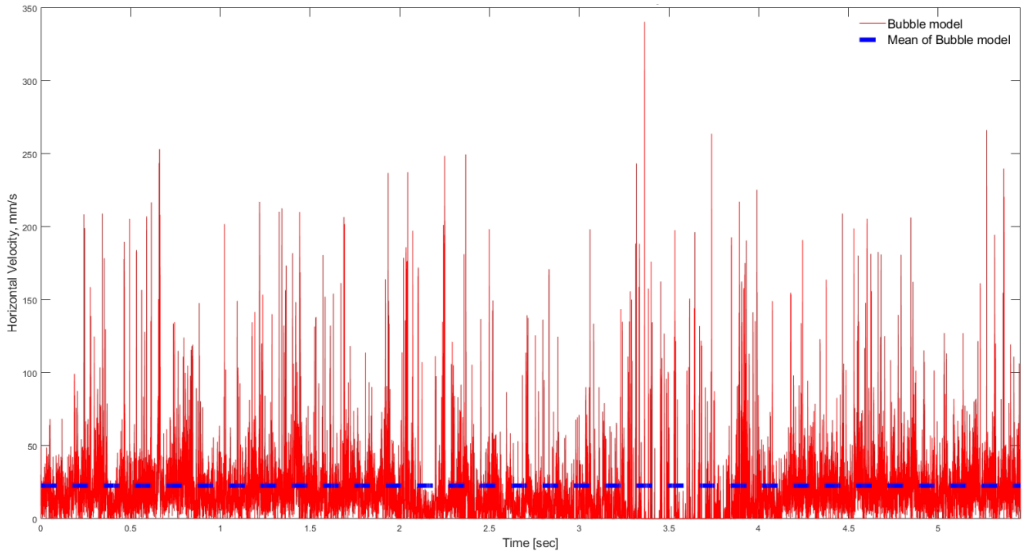
Bubble model
Mean of Bubble model
Horizontal Velocity, mm/s
Time [sec]

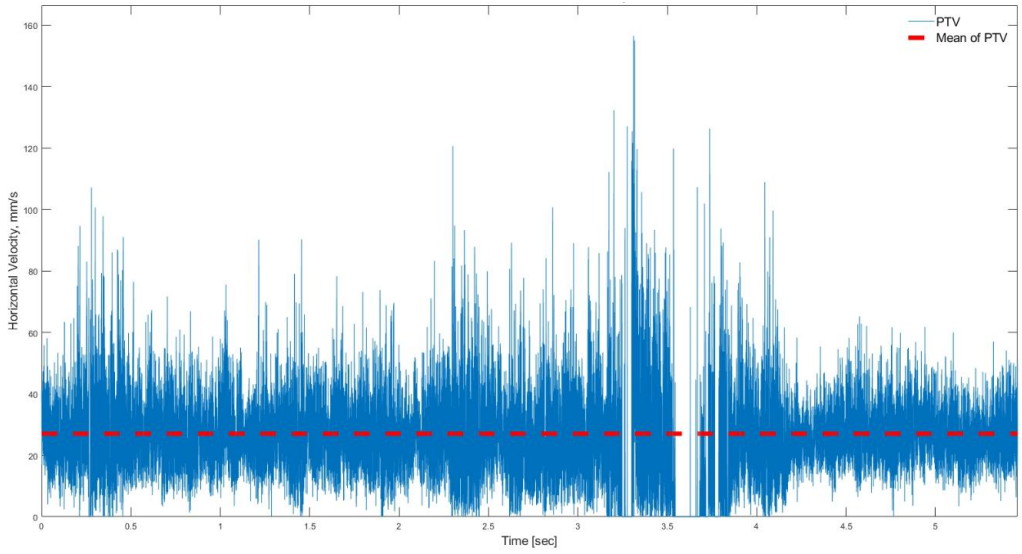
PTV
Mean of PTV
Horizontal Velocity, mm/s
Time [sec]

(a)

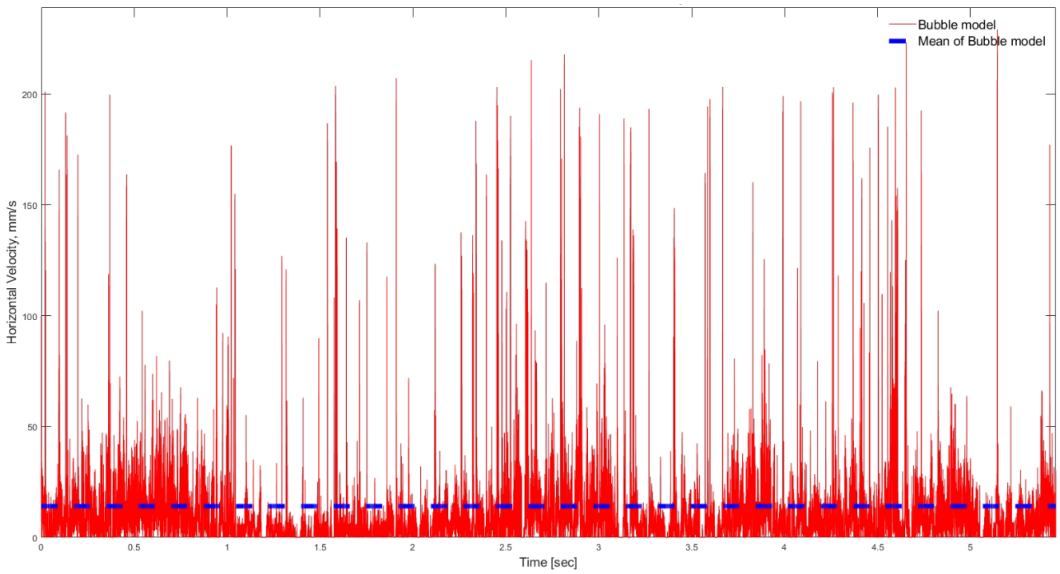
Bubble model
Mean of Bubble model
Horizontal Velocity, mm/s
Time [sec]

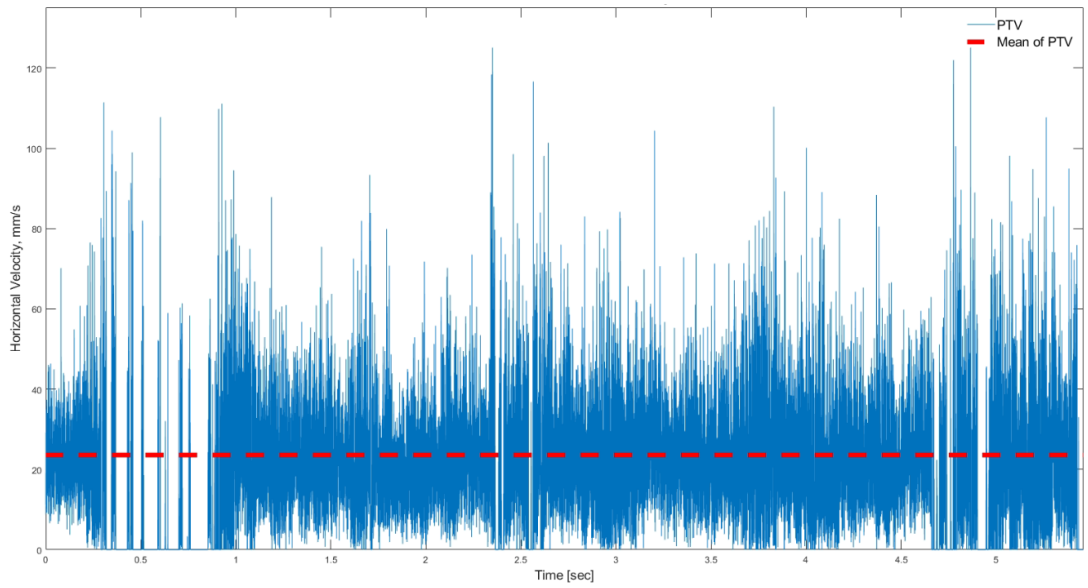
PTV
Mean of PTV
Horizontal Velocity, mm/s
Time [sec]

(b)

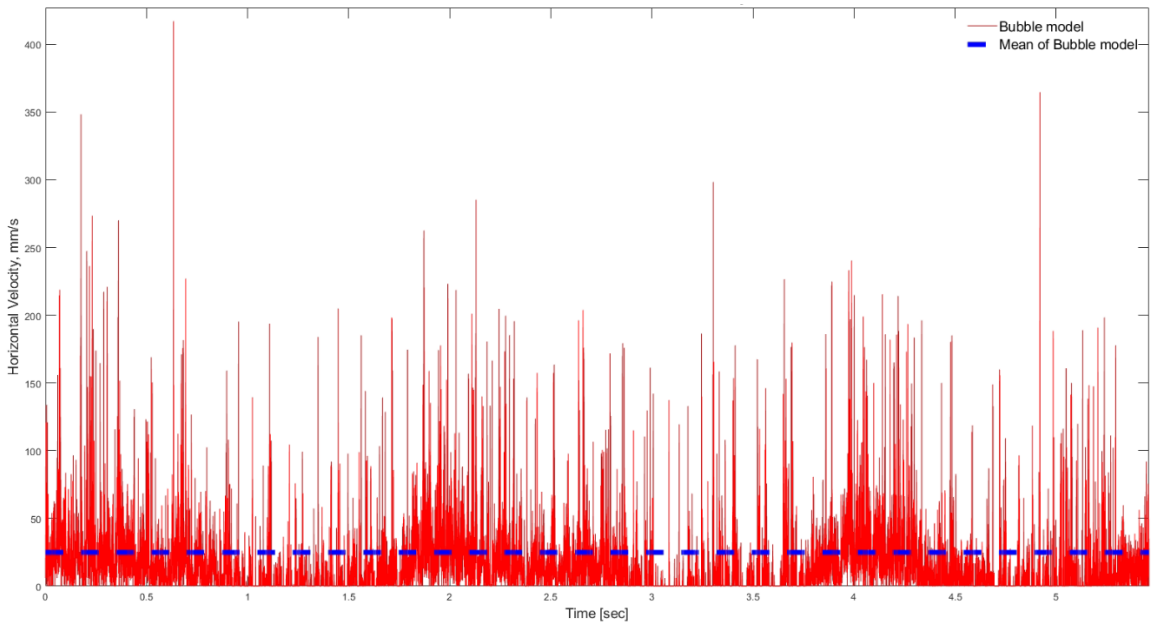
Bubble model
Mean of Bubble model
Horizontal Velocity, mm/s
Time [sec]

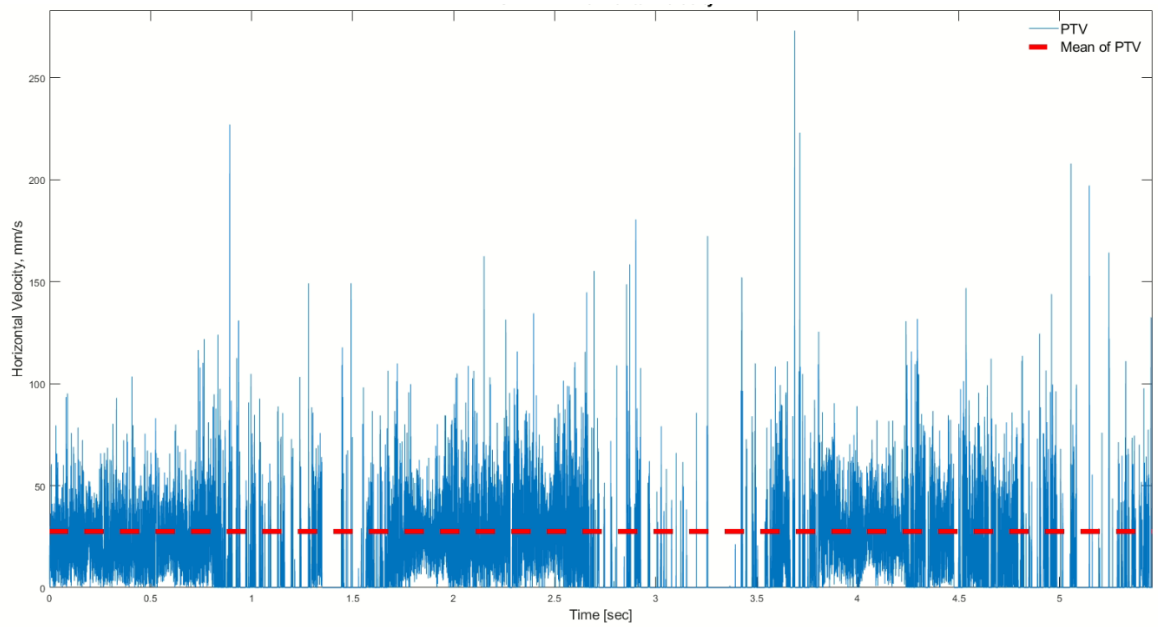
PTV
Mean of PTV
Horizontal Velocity, mm/s
Time [sec]

(c)

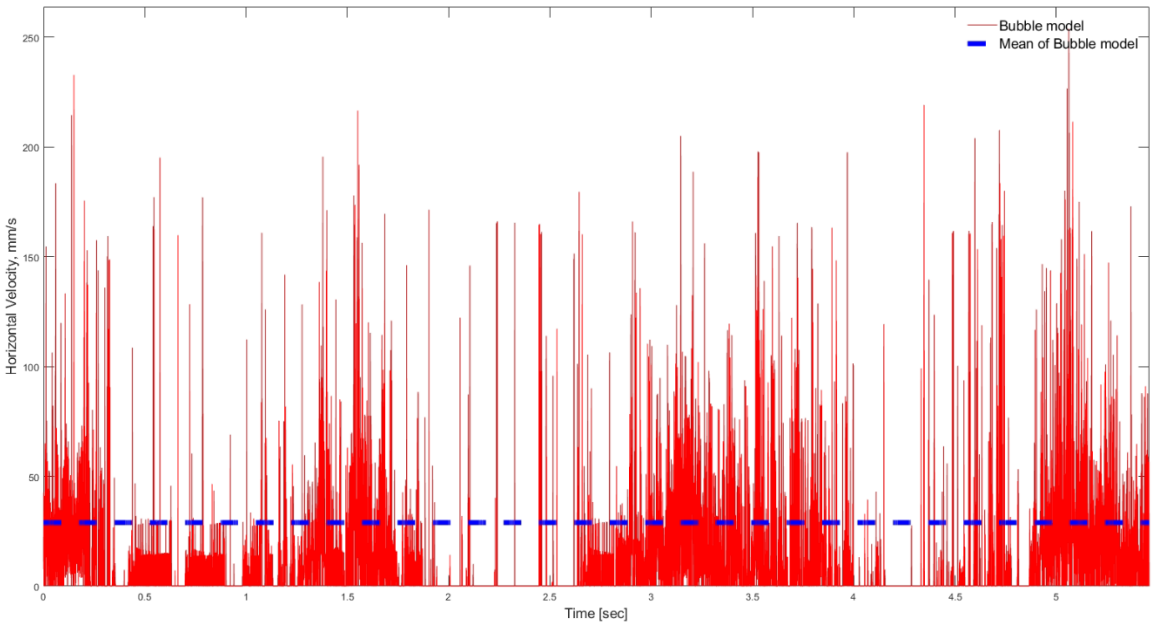

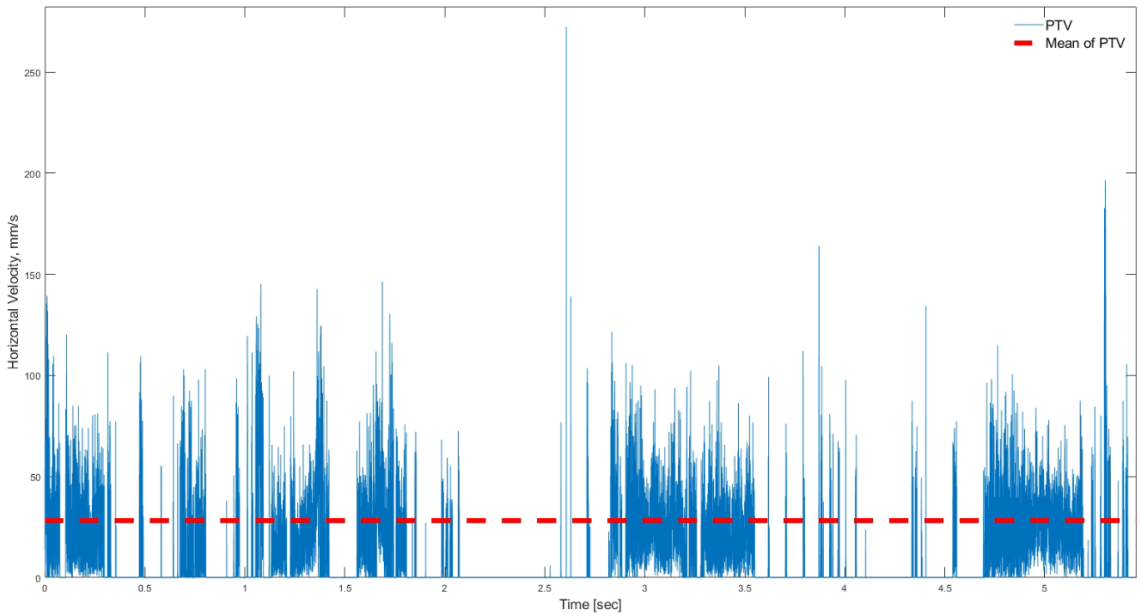

(d)

Figure 4-8: Plots of horizontal velocities obtained from semi empirical formula (red graph) and from PTV (blue graph) for different cases of subcooling and heat flux. Dotted line indicates the average velocity. (a) HSHH (b) HSMH (c) MSMH (d) LSLH

The results of horizontal velocities from the algorithm are shown in figure 4-8 for different cases of subcooling and heat flux. As mentioned previously, the low subcooling and mid-heat flux condition was not analyzed. In the plots displaying velocities using the bubble model, the velocity for each frame was calculated as a summation of velocities generated by all the growing bubbles in that frame. For the plots with particle tracking velocimetry (PTV), the velocity of each frame was an average of velocities of smaller diameter bubbles (< 1.25 mm) in that frame.

As expected, both the velocities obtained from the bubble model and those derived from particle tracking velocimetry (PTV) exhibited considerable fluctuations over time. The observed peaks in the bubble model velocities are attributed to sudden increments in either the height, diameter, or both, of bubbles attached to the ratchet in consecutive frames. This increment may arise from the merging of a bubble growing on the ratchet with other bubbles in the flow but still attached to the ratchet, as in case of HSHH and HSMH, or it may be due to rapid bubble expansion, as seen in cases like MSMH and LSLH. Additionally, the activation of more nucleation sites also contributes to higher velocities in the bubble model. The fluctuations in PTV velocities are a consequence of the fluid acceleration during periods of growth of the bubble attached to the ratchet and deceleration during waiting periods. Furthermore, PTV plots consistently exhibit zero velocity for extended durations, indicating the presence of slugs or only bubbles with diameter higher than 1.25 mm in those frames, which are not traced by the PTV algorithm. Average velocities for each case were calculated using only frames with non-zero velocities for both PTV and the bubble model. This approach eliminates frames with only bubbles of diameter higher than 1.25 mm or slugs for PTV average velocity calculation, and frames without any bubble growing on the ratchet for bubble model average velocity calculation.

As mentioned previously, Safarkoolan et al. [23] also worked on these experiment images to calculate the velocity of slugs in the flow for all the cases. Figure 4-9 shows the histogram of Bubble model horizontal velocity, PTV horizontal velocity and horizontal velocities obtained by Safarkoolan et. al. for all the cases.

The bubble model velocity and PTV average velocity are majorly distributed between 0- 50 mm/s, and the exploded view of histogram in this range is also provided. All the velocities viz. Bubble model average velocity, PTV average velocity, Average velocity of slugs, are shown in the table 4-1, table 4-2 and figure 4-10.

Table 4-1: Comparison of Horizontal Velocities of Bubble model, PTV and Slug velocity by Safarkoolan [23]

S.No.	Condition	Heat flux, W/cm^2	Sub cooling, ^0C	Average horizontal velocity – Bubble model, mm/s	Average horizontal velocity – PTV, mm/s	Error between PTV and Bubble model	Average Slug horizontal velocity – Safarkoolan, mm/s
1.	HSHH	2.47	10.52	22.72	27.04	4.32	7.62
2.	HSMH	1.40	10.8	14.08	23.59	9.51	4.63
3.	MSMH	1.48	5.7	24.97	27.56	2.60	9.77
4.	LSLH	0.86	2.3	28.94	28.16	-0.78	14.00

Table 4-2: Values of percentage of deviation of Bubble model and Slug velocity by Safarkoolan from PTV

S.No.	Condition	Bubble Model	Slug velocity - Safarkoolan
1.	HSHH	(-)15.96%	(-)71.83%
2.	HSMH	(-)40.31%	(-)80.39%
3.	MSMH	(-)9.42%	(-)64.56%
4.	LSLH	2.76 %	(-)50.29%

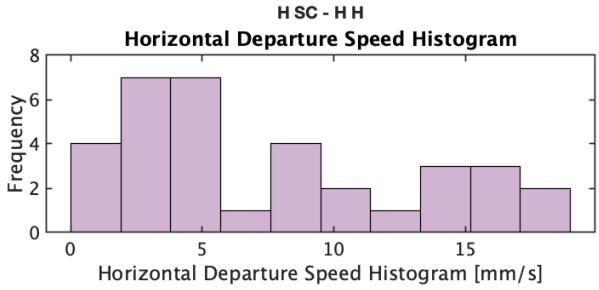
H SC - H H
Horizontal Departure Speed Histogram
Frequency
Horizontal Departure Speed Histogram [mm/s]

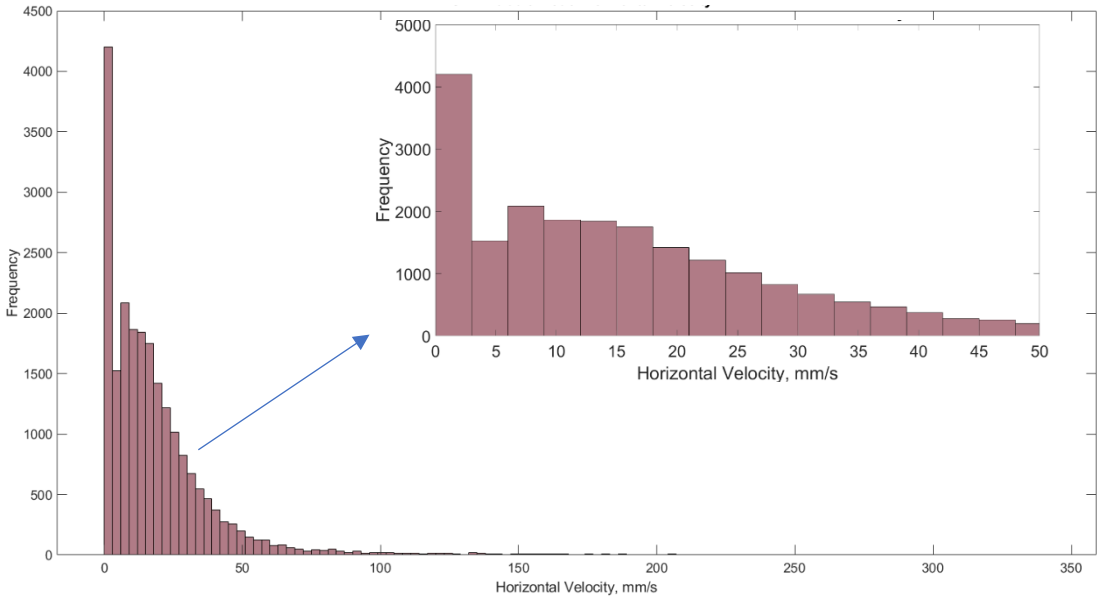
Frequency
Horizontal Velocity, mm/s

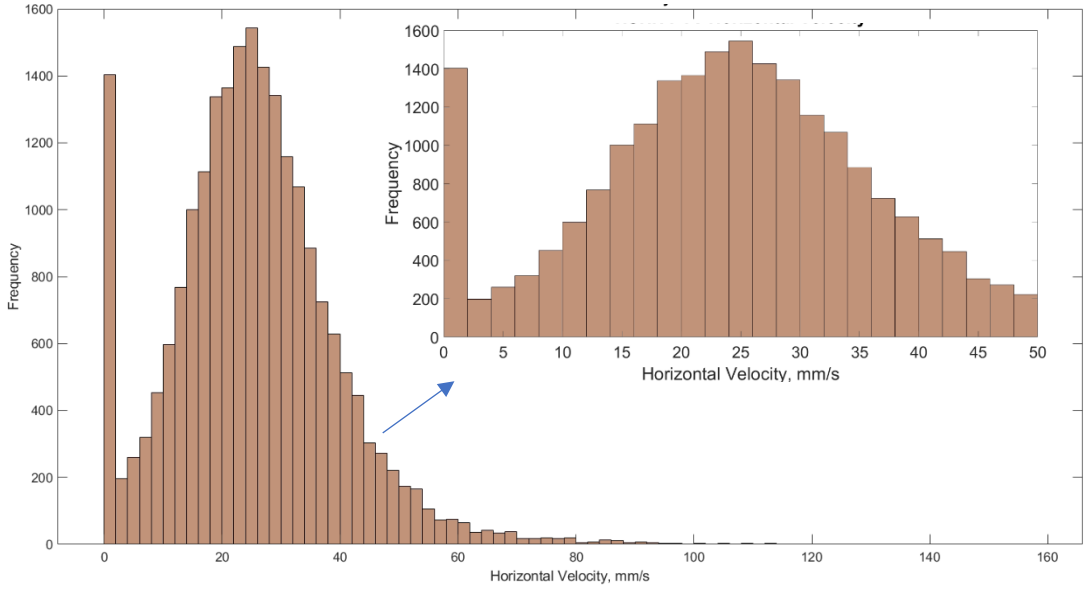
Frequency
Horizontal Velocity, mm/s

(a)

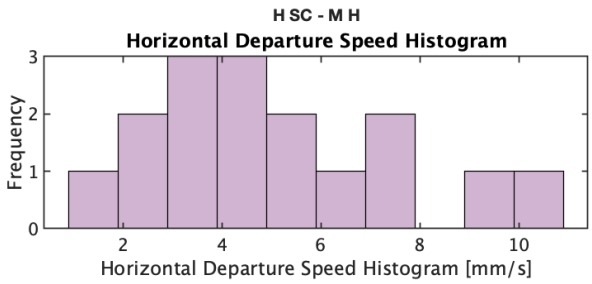
H SC - M H
Horizontal Departure Speed Histogram
Frequency
Horizontal Departure Speed Histogram [mm/s]

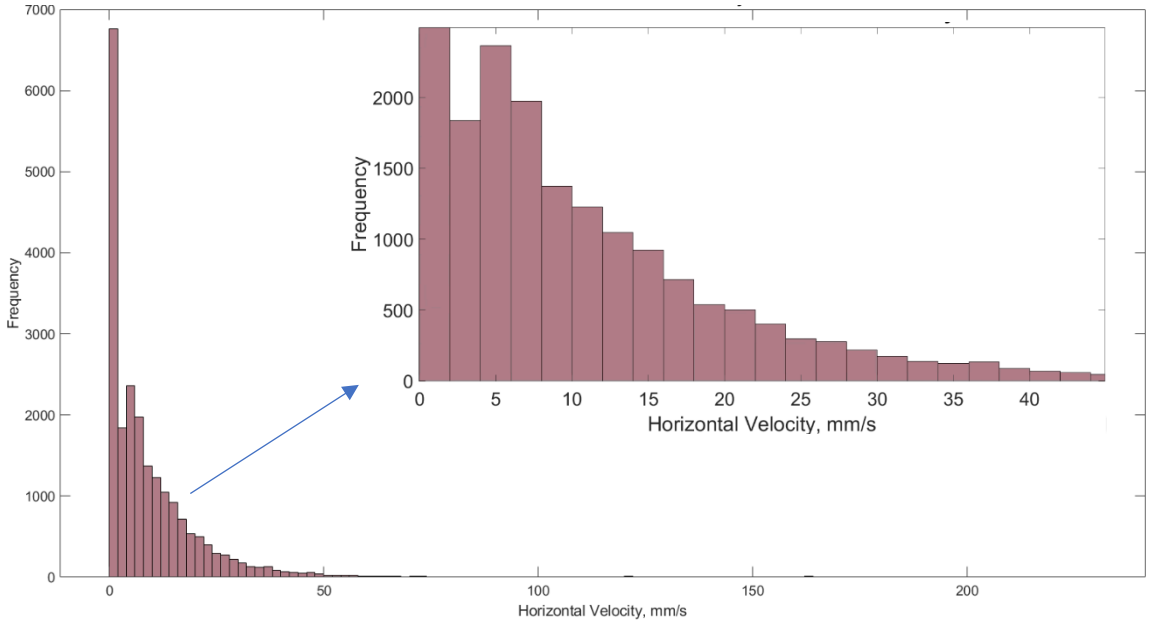
Frequency
Horizontal Velocity, mm/s
Horizontal Velocity, mm/s

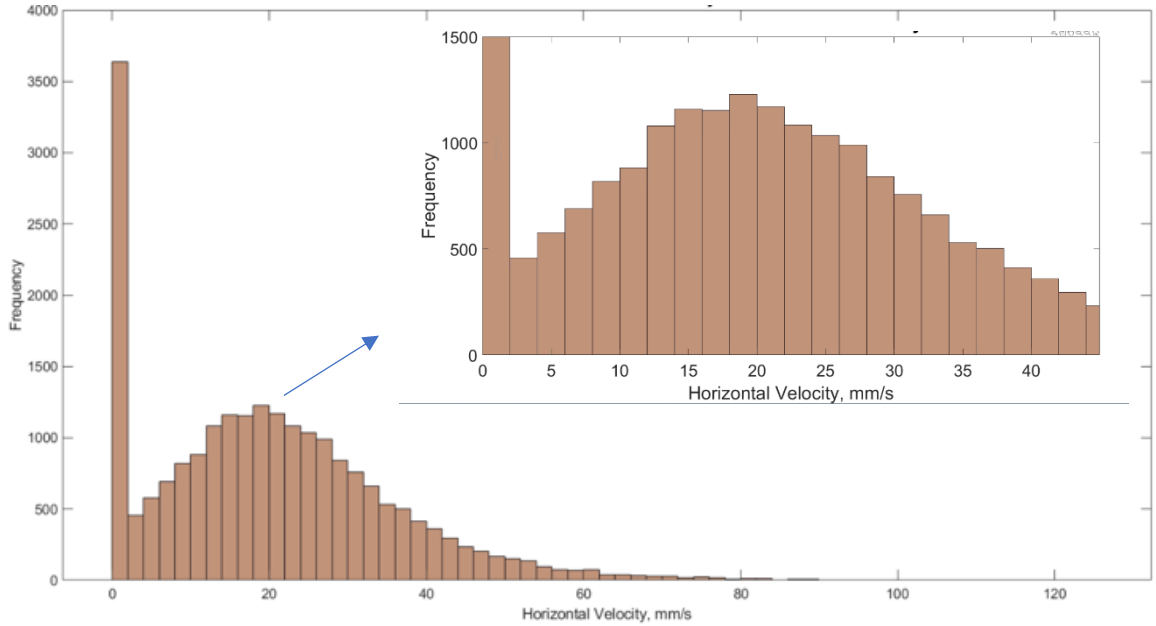
Frequency
Horizontal Velocity, mm/s
Horizontal Velocity, mm/s

(b)

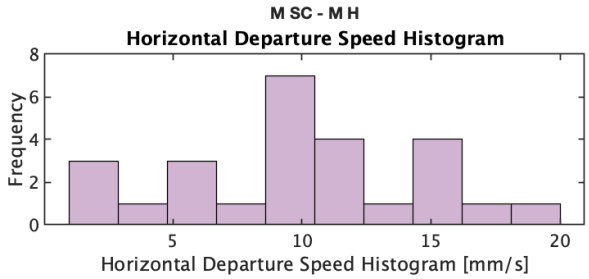
M SC - M H
Horizontal Departure Speed Histogram
Frequency
Horizontal Departure Speed Histogram [mm/s]

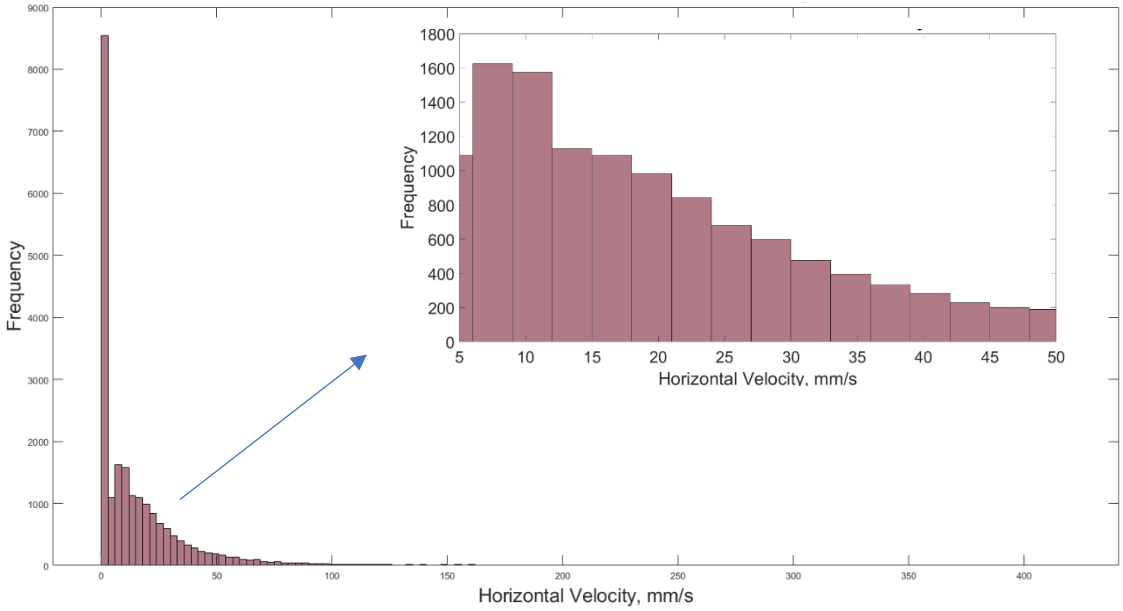
Frequency
Horizontal Velocity, mm/s
Frequency
Horizontal Velocity, mm/s

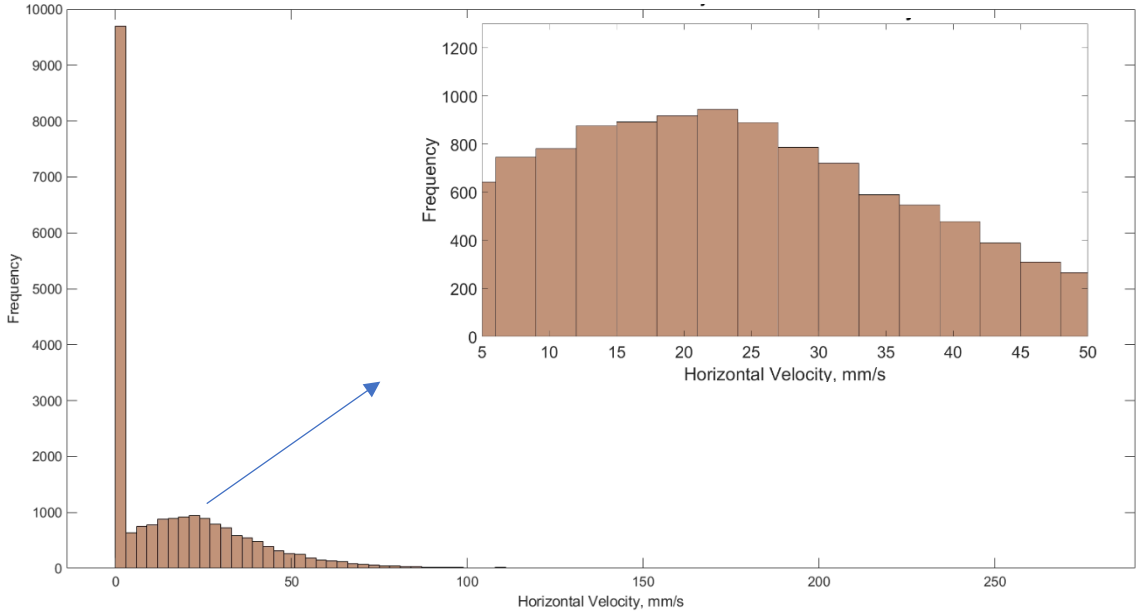
Frequency
Horizontal Velocity, mm/s
Frequency
Horizontal Velocity, mm/s

(c)

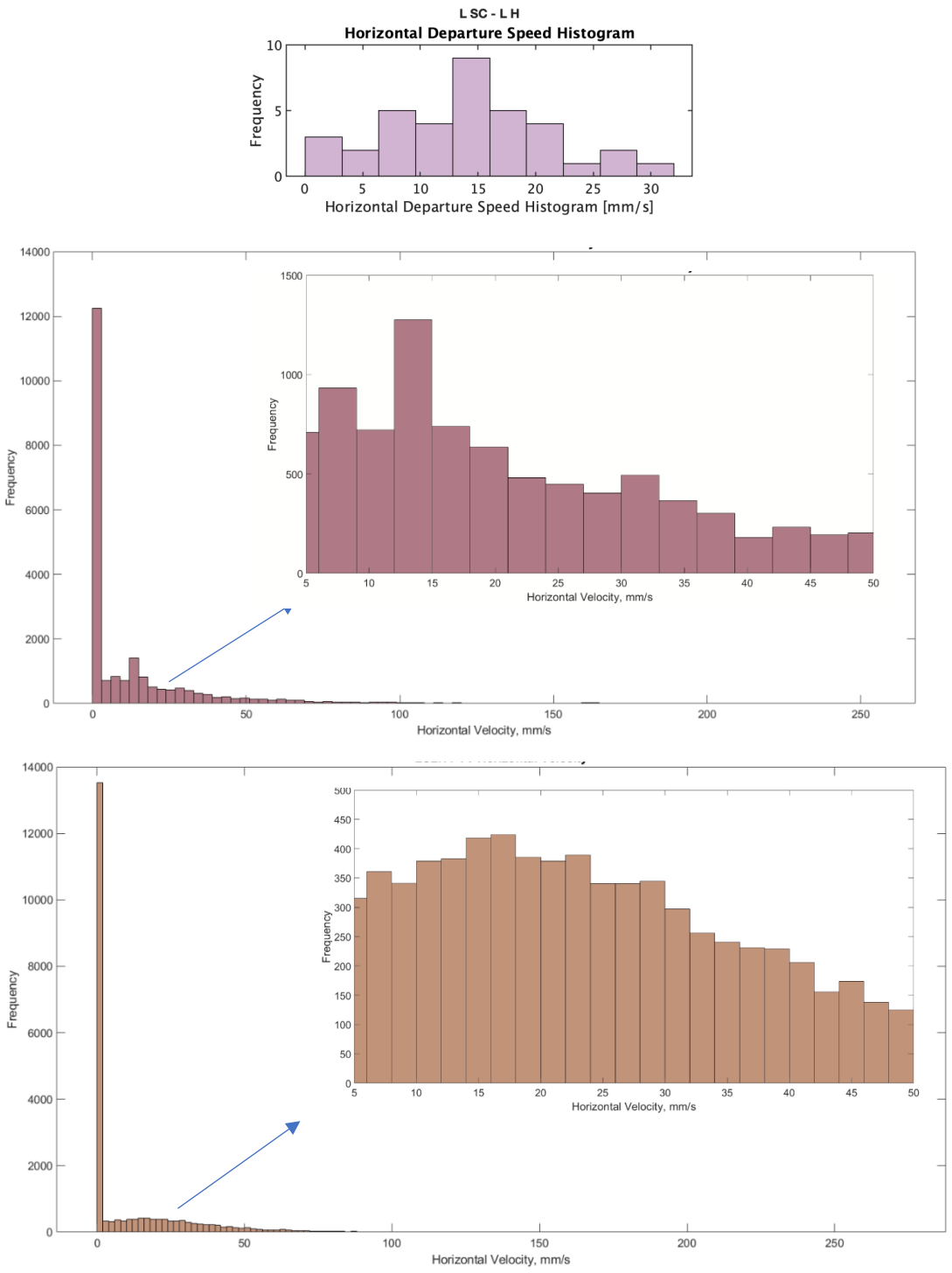

(d)

Figure 4-9: Histogram of horizontal slug velocity by Safarkoolan (at top) [23], Bubble model horizontal velocity (in the middle with exploded view from 0-50 mm/s, inside) and horizontal velocity of PTV (at bottom with exploded view from 0 to 50 mm/s inside) for all cases of subcooling and heat flux. (a) HSHH (b) HSMH (c) MSMH (d) LSLH

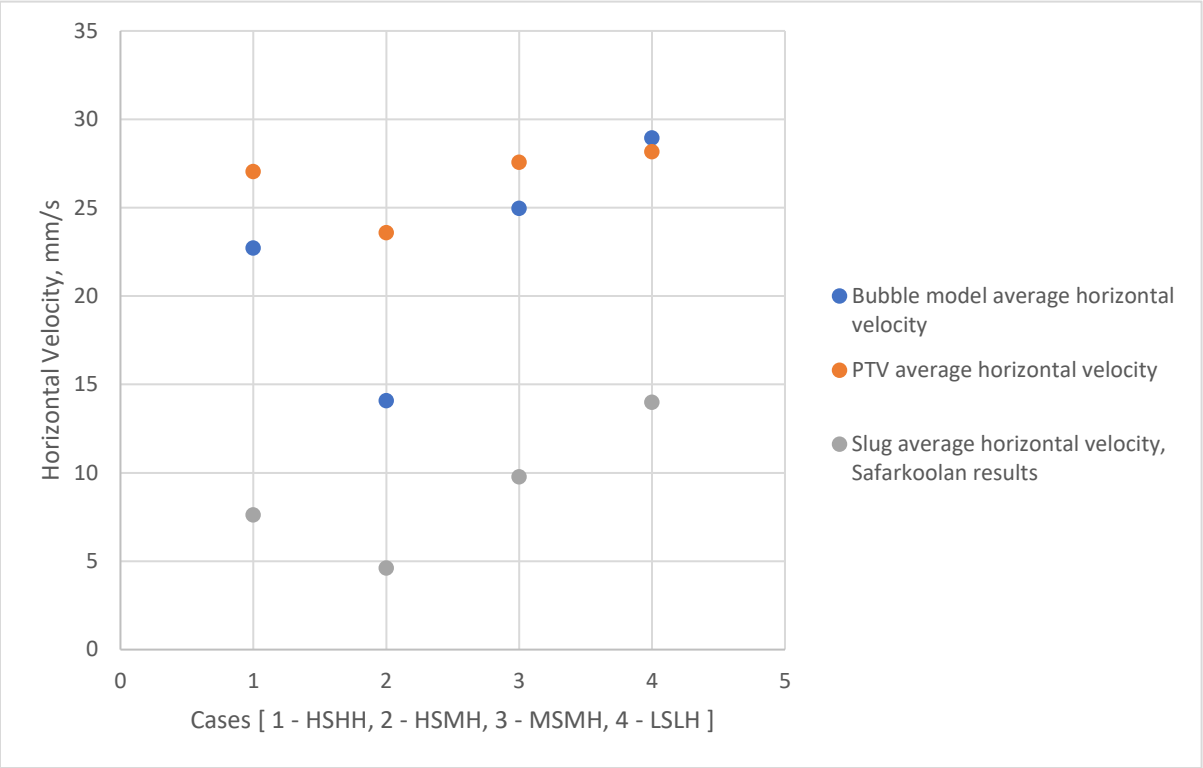

Figure 4-10: Comparison of average horizontal velocities from Bubble model, PTV, Safarkoolan results [23]

The velocities presented in table 4-1 and figure 4-10 with the velocity deviations from PTV in table 2 highlight that the horizontal velocity predicted by the bubble model's semi-empirical formula falls within the range of ± 15% of the horizontal velocity predicted by PTV, except in the case of High Subcooling and Mid Heat Flux conditions. In both the bubble model and PTV predictions, velocities exceed those anticipated by Safarkoolan. This deviation is attributed to the lower velocity of slugs due to increased drag compared to smaller bubbles in the flow. The PTV velocity, determined by smaller diameters, represents a more realistic mean flow velocity as it operates within the Stokes flow regime.

In scenarios where subcooling remains constant and heat flux varies, such as in cases like HSHH and HSMH, it is observed that the horizontal velocity predicted by the bubble model will exhibit lesser deviation from the PTV horizontal velocity with increasing heat flux. Similarly, in instances of constant heat flux and

varying subcooling, as observed in cases like HSMH and MSMH, the horizontal velocity predicted by the bubble model is observed to display reduced deviation from the PTV horizontal velocity as subcooling decreases. With a slight discrepancy between PTV velocity and bubble model velocity, in the range of ±5 mm/s for all cases except high subcooling high heat flux, the semi-empirical formula effectively predicts the lateral velocity induced by the growing bubble. This observation validates the bubble pumping technique in the nucleate boiling regime.

CHAPTER 5 CONCLUSION

An experiment was conducted to validate the hypothesis that a growing bubble on the asymmetric surface induces lateral motion in the surrounding fluid. According to the bubble growth pump model the momentum generated by the growing bubble imparts a velocity in the fluid within the bubble's area of influence. A semi empirical formula to calculate this velocity in surrounding fluid was developed using a force balance on the growing bubble by Kapsenberg[14]. The primary emphasis of the experiment was to validate this semi-empirical formula for the bubble pumping model.

A rectangular channel was created by vertically placing two ratchets, each featuring "hammered-shaped" reentrant slots and positioned opposite to each other. Serpentine heaters, located at the rear side of the ratchets, were used to supply the required heat flux, while cooling loops integrated into the test chamber facilitated the control of subcooling. The experiment was conducted within the nucleate boiling regime, with six distinct cases of varying heat flux and subcooling conditions ranging from 0.86-2.47 W/cm² and 2.3–10.52 °C, respectively. Specifically, one of the cases involved the rotation of the ratchets by 180 degrees, undertaken to validate whether the growing bubble on the ratchet induces a preferential directional motion in the surrounding fluid.

The high-speed images obtained from the experiments were analyzed to determine the bubble growth. Image processing techniques were used to extract the data such as height and diameter of the bubble growing on the ratchet in each frame. The horizontal velocity imparted by the growing bubble on the ratchet in the surrounding fluid was obtained using this bubble growth data and the semi empirical formula. Particle tracking velocimetry (PTV) techniques were used to measure liquid velocities in the flow. Small bubbles falling within the Stoke's flow regime were tracked to determine the mean velocity of the flow in each frame. The horizontal component of this mean velocity of the flow from PTV was compared

with the average horizontal velocity obtained from the semi empirical formula to validate the bubble pumping model.

The comparative analysis demonstrated that the semi-empirical formula consistently predicts horizontal velocities within a tolerance of ±5 mm/s of the horizontal velocities determined by Particle Tracking Velocimetry (PTV), except for the high subcooling mid-heat flux condition. Specifically, the semi-empirical formula resulted horizontal velocities with deviations of -15.96%, -9.42%, and 2.76% from the horizontal velocities determined by PTV for high subcooling high heat flux, mid subcooling mid heat flux, and low subcooling low heat flux conditions, respectively. Notably, in the case of high subcooling mid-heat flux, the deviation was very high, reaching -40%. For constant subcooling, the semi-empirical formula exhibited improved velocity predictions, as the heat flux applied increases. Conversely, under constant heat flux, the formula achieved better velocity predictions with reduced subcooling.

In summary, the growing bubble on the ratchet induced an average horizontal velocity ranging from 20 to 30 mm/s in the surrounding liquid. Qualitative visualization under conditions of high heat flux and high subcooling, with ratchets turned 180 degrees, revealed an opposite direction of fluid movement compared to other conditions. Collectively, these findings confirm that the growing bubble on the ratchet imparts a preferential direction of lateral motion in the surrounding fluid. Furthermore, the results indicate that the semi-empirical formula effectively predicts the velocity imparted by the growing bubble in this experimental setup.

CHAPTER 6 RECOMMENDATIONS FOR FUTURE INVESTIGATIONS

The algorithm developed for image analysis encountered difficulties in accurately segmenting closely located bubbles. Further refinement of the algorithm is essential to precisely determine bubble height and diameter, considering their critical influence on the final velocity calculation using the semi-empirical formula. The algorithm also faced challenges in analyzing the low subcooling and mid-heat flux condition. This limitation is due to the algorithm's inability to differentiate between the slug covering the entire ratchet area and the bubbles nucleating and merging with this slug. To address these complexities, more sophisticated and sensitive models utilizing machine learning should be developed, offering a more effective and comprehensive understanding of two-phase flow in such intricate scenarios.

The semi-empirical formula resulted in a higher deviation from Particle Tracking Velocimetry (PTV) velocity predictions in the case of high heat flux and mid-subcooling conditions. Further investigation is required to understand the underlying reasons for this deviation and the governing principles of the flow in such condition. A detailed study of this specific condition will contribute to a more comprehensive understanding of the dynamics involved and may guide refinements or adjustments to the semi-empirical formula for improved accuracy in predicting velocities.

Various parameters, including test channel width, pitch of the ratchet, nucleation site location, orientation of ratchets, among others, are expected to influence the velocity imparted by the growing bubble in the surrounding fluid. A comprehensive parametric study should be undertaken to systematically investigate and understand the impact of these parameters. This study will contribute valuable insights into the relationships between these factors and the resulting fluid dynamics, providing a foundation for optimizing the experimental setup and refining theoretical models for enhanced predictive accuracy.

REFERENCES

[1] T. L. Bergman, A. S. Lavine, F. P. Incropera, and D. P. DeWitt, *Introduction to Heat Transfer*. John Wiley & Sons, 2011.

[2] Y. A. Çengel, *Heat Transfer: A Practical Approach*. McGraw-Hill, 2003.

[3] V. P. Carey, *Liquid-Vapor Phase-Change Phenomena: An Introduction to the Thermophysics of Vaporization and Condensation Processes in Heat Transfer Equipment, Third Edition*, 3rd ed. Boca Raton: CRC Press, 2020. doi: 10.1201/9780429082221.

[4] G. Liang and I. Mudawar, "Review of channel flow boiling enhancement by surface modification, and instability suppression schemes," *Int. J. Heat Mass Transf.*, vol. 146, p. 118864, Jan. 2020, doi: 10.1016/j.ijheatmasstransfer.2019.118864.

[5] H. Jouhara, A. Chauhan, T. Nannou, S. Almahmoud, B. Delpech, and L. C. Wrobel, "Heat pipe based systems - Advances and applications," *Energy*, vol. 128, pp. 729–754, Jun. 2017, doi: 10.1016/j.energy.2017.04.028.

[6] Zhang, Hongzhe, Fang Ye, Hang Guo, and Xiaoke Yan. 2022. "Isothermal Performance of Heat Pipes: A Review" Energies 15, no. 6: 1992. https://doi.org/10.3390/en15061992

[7] I. Voigt and W.-G. Drossel, "Experimental investigation of heat pipe performance under translational acceleration," *Heat Mass Transf.*, vol. 58, no. 2, pp. 209–219, Feb. 2022, doi: 10.1007/s00231-021-03106-w.

[8] P. Nemec, A. Čaja, and M. Malcho, "Mathematical model for heat transfer limitations of heat pipe," *Math. Comput. Model.*, vol. 57, no. 1, pp. 126–136, Jan. 2013, doi: 10.1016/j.mcm.2011.06.047.

[9] P. B. C. Von and M. C. Georg, "Refrigeration," US1669269A, May 08, 1928 Accessed: Dec. 06, 2023.

[10] B. Gurevich, “Bubble Pump Models Verification Based on the Experimental Results,” presented at the The 3rd World Congress on Mechanical, Chemical, and Material Engineering, Jun. 2017. doi: 10.11159/htff17.113.

[11] “Modelling of heat flux received by a bubble pump of absorption-diffusion refrigeration cycles | Heat and Mass Transfer.”

[12] N. Ben Ezzine, R. Garma, M. Bourouis, and A. Bellagi, “Experimental studies on bubble pump operated diffusion absorption machine based on light hydrocarbons for solar cooling,” *Renew. Energy*, vol. 35, no. 2, pp. 464–470, Feb. 2010, doi: 10.1016/j.renene.2009.07.026.

[13] H. Linke *et al.*, “Self-Propelled Leidenfrost Droplets,” *Phys. Rev. Lett.*, vol. 96, no. 15, p. 154502, Apr. 2006, doi: 10.1103/PhysRevLett.96.154502.

[14] F. Kapsenberg, L. Strid, N. Thiagarajan, V. Narayanan, S.H. Bhavnani, On the lateral fluid motion during pool boiling via preferentially located cavities, Appl. Phys. Lett., 104 (2014), p. 154105

[15] L. Strid, “Passive pumping in pool and open channel configurations via meso-scale asymmetric surface patterning.”

[16] K. Sridhar, V. Narayanan, and S. H. Bhavnani, “Asymmetric Sawtooth Microstructure-Induced Vapor Mobility for Suppressed Buoyancy Conditions: Terrestrial Experiment and Design for ISS Experiments,” *IEEE Trans. Compon. Packag. Manuf. Technol.*, vol. 11, no. 10, pp. 1625–1633, Oct. 2021, doi: 10.1109/TCPMT.2021.3104467.

[17] Y.-F. Xue, J.-F. Zhao, J.-J. Wei, J. Li, D. Guo, and S.-X. Wan, “Experimental Study of Nucleate Pool Boiling of FC-72 on Smooth Surface under Microgravity,” *Microgravity Sci. Technol.*, vol. 23, no. 1, pp. 75–85, Sep. 2011, doi: 10.1007/s12217-011-9274-5.

[18] Thiagarajan N, Bhavnani SH, Narayanan V. Self-propelled sliding bubble motion induced by surface microstructure in pool boiling of a dielectric fluid under microgravity. J Electron Package. 2015; 137(2):021009.

[19] S. Bhavnani, V. Narayanan, N. Thiagarajan, and L. Strid, “PASSIVE DIRECTIONAL MOTION OF FLUID DURING BOILING DRIVEN BY SURFACE ASYMMETRY IN A DIELECTRIC FLUID,” *J. Enhanc. Heat Transf.*, vol. 26, no. 4, 2019, doi: 10.1615/JEnhHeatTransf.2019027652.

[20] Youngjoon Suh, Sanghyeon Chang, Peter Simadiris, Tiffany B. Inouye, Muhammad Jahidul Hoque, Siavash Khodakarami, Chirag Kharangate, Nenad Miljkovic, Yoonjin Won, VISION-iT: A Framework for Digitizing Bubbles and Droplets, Energy and AI, Volume 15, 2024, 100309, ISSN 2666-5468, https://doi.org/10.1016/j.egyai.2023.100309.

[21] Safarkoolan, R. "“Assessment of Thermally Actuated Pumping in an Open-ended Channel with Multi-Scale Surface Asymmetry,” virtual, July 12-15, 2020". 18th International Conference on Nanochannels, Microchannels, and Minichannels.

[22] M. Krstić, “MIXING CONTROL FOR JET FLOWS,” in *Combustion Processes in Propulsion*, Elsevier, 2006, pp. 87–96. doi: 10.1016/B978-012369394-5/50013-5.

[23] R. Safarkoolan, R. Odele, V. Narayanan, and S. H. Bhavnani, “Poster presentation, mFIP conference, Quantitative Visualization of Thermally Actuated Pumping in an Open-ended Channel with Surface Asymmetry and Reentrant Slot Cavities.”

APPENDICES

Appendix A. FC – 72 Properties

Courtesy of 3M website

$\rho = 1740 - (2.61*T)$

$\rho = [kg/m^3]$; $T = [^0C]$

Saturated data for FC-72

T [K]	P [bar]	T [K]	P [bar]
250	0.018	302	0.358
252	0.021	304	0.389
254	0.025	306	0.422
256	0.028	308	0.458
258	0.033	310	0.496
260	0.038	312	0.536
262	0.043	314	0.579
264	0.049	316	0.624
266	0.056	318	0.672
268	0.063	320	0.723
270	0.071	322	0.777
272	0.080	324	0.833
274	0.090	326	0.893
276	0.101	328	0.956
278	0.113	330	1.023
280	0.126	332	1.093
282	0.140	334	1.166
284	0.155	336	1.243
286	0.171	338	1.324
288	0.189	340	1.410
290	0.208	342	1.499
292	0.229	344	1.592
294	0.251	346	1.691
296	0.275	348	1.793
298	0.301	350	1.901
300	0.328	352	2.013

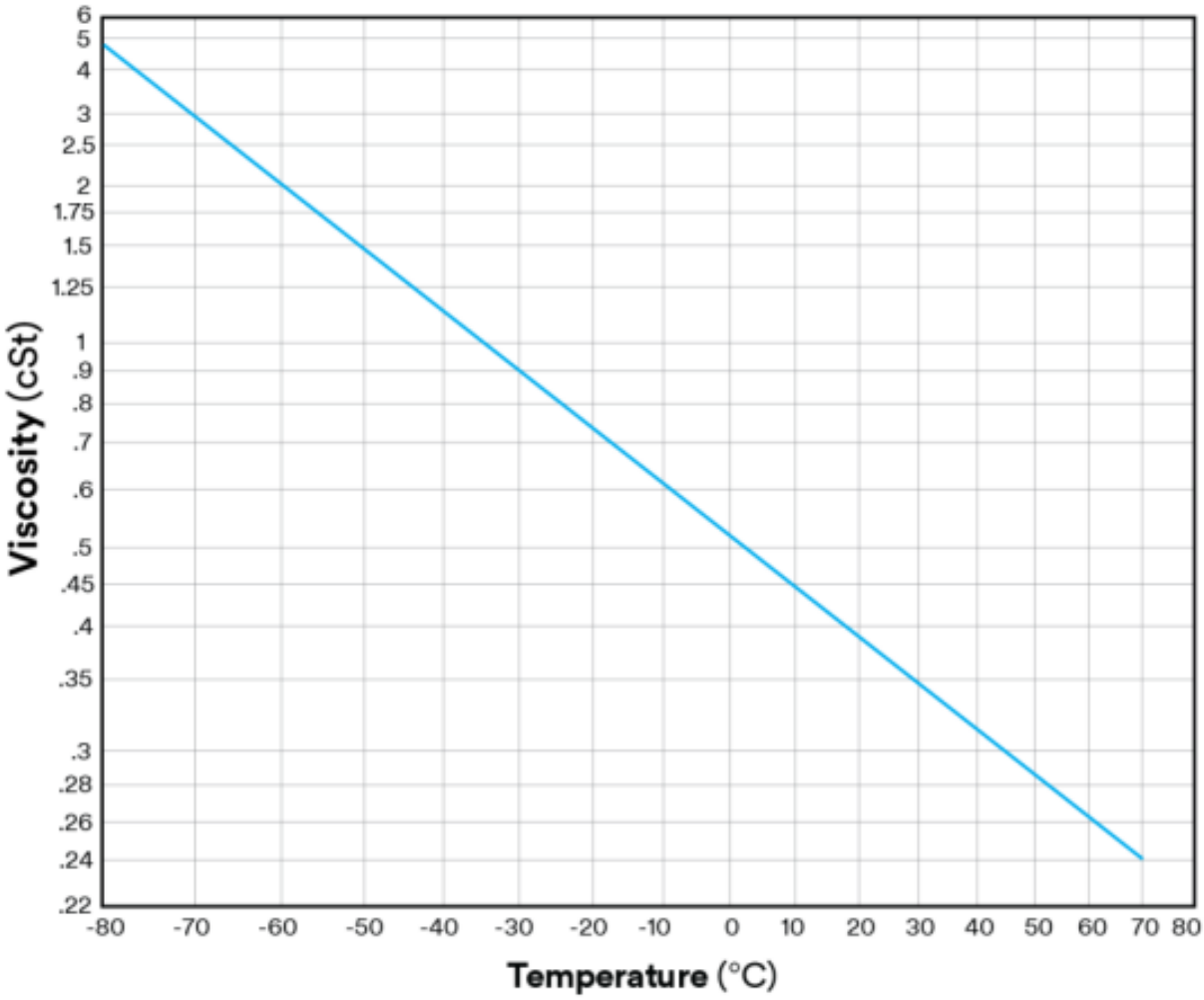

FC 72 Viscosity vs. Temperature